Kim *et al. Soft Sci* 2024;4:33
DOI: 10.20517/ss.2024.28

Soft Science

Review Article

Open Access

Check for updates

Transparent *p*-type copper iodide for next-generation electronics: fundamental physics and recent research trends

Ga Hye Kim[#], Jiyong Lee[#], Kyunghan Ahn, Myung-Gil Kim[*]

School of Advanced Materials Science and Engineering, Sungkyunkwan University, Suwon 16419, Republic of Korea.
[#]Authors contributed equally.

Correspondence to: Prof. Myung-Gil Kim, School of Advanced Materials Science and Engineering, Sungkyunkwan University, 2066 Seobu-ro, Jangan-gu, Suwon 16419, Republic of Korea. E-mail: myunggil@skku.edu

How to cite this article: Kim GH, Lee J, Ahn K, Kim MG. Transparent *p*-type copper iodide for next-generation electronics: fundamental physics and recent research trends. *Soft Sci* 2024;4:33. https://dx.doi.org/10.20517/ss.2024.28

Received: 2 Jul 2024 **First Decision:** 6 Aug 2024 **Revised:** 25 Aug 2024 **Accepted:** 3 Sep 2024 **Published:** 14 Sep 2024

Academic Editor: Zhigang Chen **Copy Editor:** Pei-Yun Wang **Production Editor:** Pei-Yun Wang

Abstract

Development of transparent and flexible *p*-type semiconductors has been a significant challenge for scientific curiosity and industrial interest. Unlike *n*-type metal oxide semiconductors, such as zinc oxide (ZnO), In_2O_3, and SnO_2, transparent *p*-type oxide semiconductors have suffered from low optical transparency and poor electrical performance. To overcome the intrinsic limitation of *p*-type oxide semiconductors, copper iodide (CuI) is gaining attention as a multifunctional *p*-type semiconductor with excellent optical transparency, decent mechanical flexibility, high hole mobility, high electrical conductivity, and even promising thermoelectric performance. Here, we present the recent progress of CuI-based transparent *p*-type electronics from materials to applications. In this review, we summarize the physical and chemical properties of CuI by reviewing computational studies, focusing on the band structure, intrinsic defects, and promising dopants. Additionally, various applications of CuI, including its use as active layers, hole transport layers (HTLs), transparent electrodes, and energy harvesters, are examined, highlighting important studies and their findings. Strategies to enhance device performance, such as controlling carrier concentrations and refining fabrication methods, are discussed, offering insights for developing next-generation electronic devices. Finally, we discuss current challenges and perspective opportunities of CuI-based transparent *p*-type electronics.

Keywords: Copper iodide, *p*-type semiconductor, optoelectronic materials, transparent conductive electrodes, transparent energy harvesting materials

INTRODUCTION

The continuous development of large area electronic devices requires innovations of materials in form factors, optical transparency, and multifunctionality for emerging applications such as flexible/stretchable displays, smart windows, transparent energy harvesters, and computing systems on plane[1-4]. Conventional silicon-based semiconductors cannot satisfy these needs, making the development of advanced semiconductors necessary. *n*-Type metal oxide semiconductors are highly transparent (T_{vis} > 90%), physically robust, and exhibit high electrical performances [electron mobility (μ_e) > 50 $cm^2 \cdot V^{-1} \cdot s^{-1}$ and conductivity > 5,000 $S \cdot cm^{-1}$][5,6]. However, the lack of available *p*-type semiconductors limits the potential for new forms of complementary large area electronic devices[7].

Considerable efforts have been directed towards realizing large area compatible flexible and transparent *p*-type semiconductors. Although the conduction band maximum (CBM) of *n*-type metal oxides composed of spherical and largely dispersed metal n*s* orbitals resulting in small effective masses and suitable pathways for electrons, the valance band minimum (VBM) of typical metal oxides mainly comprises oxygen (O) 2*p* orbital. The O 2*p* orbital is anisotropic and localized, leading to relatively large effective masses and low hole mobility (μ_h). Moreover, while the O vacancies in *n*-type oxide semiconductors act as facile donors, the metal vacancy in *p*-type oxide semiconductors usually results in a deep level trap rather than acting as facile acceptors. To relieve the anisotropic and localized characteristics of the O 2*p* orbital in metal oxide semiconductors, the hybridization concept at the VBM was proposed by Kawazoe *et al.* The hybridization of the metal (n-1)*d* orbital with the energy levels of an anion (such as O) at the VBM can enhance orbital overlap, reduce hole effective mass, and subsequently facilitate hole transport[8-10]. Following this concept, metal oxides such as Cu_xO, SnO, zinc oxide (ZnO), and NiO were developed[11]. However, compared to the *n*-type counterparts, the *p*-type oxides still struggle with high effective mass, low transmittance, unstable chemical states, or poor electrical conductivity.

Copper iodide (CuI) is a promising alternative for *p*-type metal oxides, having high electrical properties, optical transmittance, and even flexibility. Iodine has smaller electronegativity and size than O, resulting in more delocalization of pseudo-spherical 5*p* orbitals at the VBM[12]. Consequently, CuI could possess low hole effective mass (m_h^*) and high μ_h[13,14]. Metal oxides do not inherently satisfy flexible properties, but strategies such as creating thin metal oxide layers[15,16], multi-layers[17-20], nanostructures[21-23], or mixing with other flexible materials such as organics and polymers[24-26], making them suitable for flexible electronic devices. However, with a relatively lower Young's modulus of 36.6 GPa for CuI than the very rigid Young's modulus of 118 GPa for Sn-doped In_2O_3 (ITO), CuI has demonstrated flexible characteristics in various applications[27-31]. Moreover, the low processing temperature of CuI thin films and their adaptability to various fabrication methods make them easy to deposit on flexible substrates. In addition, the μ_h of CuI is reported as 43.9 $cm^2 \cdot V^{-1} \cdot s^{-1}$ in the single grain, and carrier concentration ranges from 10^{17} to 10^{19} cm^{-3}, attributed to copper vacancies[14,32]. The direct bandgap of CuI is 3.1 eV, resulting in transmittance in the visible region of over 80%[12,33]. CuI can be fabricated using various methods such as solution process[33-35], vacuum process[36-38], and iodination process[28,39], making it suitable for industry. It also exhibits reasonable stability compared to other halide materials[40]. Therefore, we suggest CuI as a promising *p*-type semiconductor counterpart to *n*-type metal oxides such as ITO and In-Ga-Zn-O (IGZO) for next-generation electronic devices, offering high electrical properties, high transmittance, and flexibility.

In this review, we discuss the recent advances of CuI as a transparent, flexible, and high-performance *p*-type semiconductor, focusing on its physical and electrical properties. First, we briefly summarize the various fabrication methods for CuI. Then, we overview theoretical and experimental studies to understand the fundamental electrical characteristics of CuI, such as limitations of mobility, nature of defects, and possible

dopants. There have been intensive research efforts on tuning of carrier concentration for target applications, such as reduction, increase, and optimization of hole concentration for thin-film transistors (TFTs), transparent conducting electrodes (TCEs), and thermoelectric generators (TEGs), respectively. As interest in CuI increases as a transparent *p*-type semiconductor, we summarize recent progress on diverse applications, such as diodes, channel layers for TFTs, TCEs, hole transport layers (HTLs) for optoelectronic devices, and thermoelectric devices, as well as its flexibility and stability of each device. Finally, we will discuss current challenges and outlook for the successful industrial implementation of CuI as a *p*-type transparent semiconductor.

FABRICATION METHODS OF COPPER IODIDE

In 1907, Bädeker reported CuI with vapor iodination as the first transparent electrode[41]. As a promising transparent *p*-type semiconductor, extensive research has been conducted for enhancement of carrier mobility, control of surface morphology and crystallinity, optimization of carrier concentration, cost-effective fabrication methods, and realization of various electronic devices [Figure 1]. CuI can be fabricated with various methods, making it suitable for industrial applications. These methods include solution process, vacuum process, and iodination process, allowing CuI to be easily formed into polycrystalline thin films. For the solution process, techniques such as spin-coating and spray-coating are used. Spin-coated CuI has shown high transistor performance by controlling film thickness through annealing or doping to decrease carrier concentration[42]. The selection of an appropriate solvent, such as acetonitrile (ACN), dimethyl sulfoxide (DMSO), or a co-solvent mixture of ACN and ethanolamine, is also crucial[34,43]. The mechanical and chemical vulnerability of CuI with weak ionic bonding between Cu^+ and I^- hinder facile patterning of CuI thin-film with standard photolithography processes. To overcome the challenges, direct pattering of CuI thin-films was demonstrated with inkjet printing[44] and spray-coating over stencil mask[45].

The conventional deposition method of CuI thin-films in industry is vacuum processes, such as sputtering, thermal evaporation, and pulsed laser deposition (PLD), which are beneficial for large-scale manufacturing with facile control of film thickness, large area uniformity, and compatibility to other layers without damage from processing solvents. PLD is a favorable method for depositing high-purity films and maintaining stoichiometry due to the high power laser and its ability to vaporize CuI with high energy in a short time[38]. Sputtered CuI thin films exhibit high electrical conductivity and transmittance[39]. To control the carrier concentration of sputtered CuI thin-film, dopants can be introduced by using alloy target or ion implantation into the CuI films[46,47]. Including reactive evaporation of Cu with I_2 vapor, thermal evaporation of CuI is favored for its ease of operation[48].

Iodination method is a straightforward way to fabricate CuI films by converting Cu or precursor films to CuI. When Cu, Cu_3N[39], or Cu_2S[49] thin-film is exposed to an iodine-rich environment, a spontaneous iodination process occurs, regardless of an iodine state (vapor, solid, or dissolved in solvent). Vapor iodination involves placing Cu precursor films and small iodine particles in a closed system until the process is complete, usually within 1 h. This method is simple but controlling iodine concentration can be challenging, especially at low temperatures, although heating the container with iodine particles helps. Solid iodination has been reported to convert Cu_3N to CuI with higher transmittance than vapor iodination by Yamada *et al.*[39]. In liquid iodination, non-polar solvents such as hexane result in good morphology and high electrical conductivity. Ahn *et al.* found that liquid iodination reduces doping formation energy compared to vapor iodination and allows facile control of iodine concentration by adjusting the solution's concentration[28].

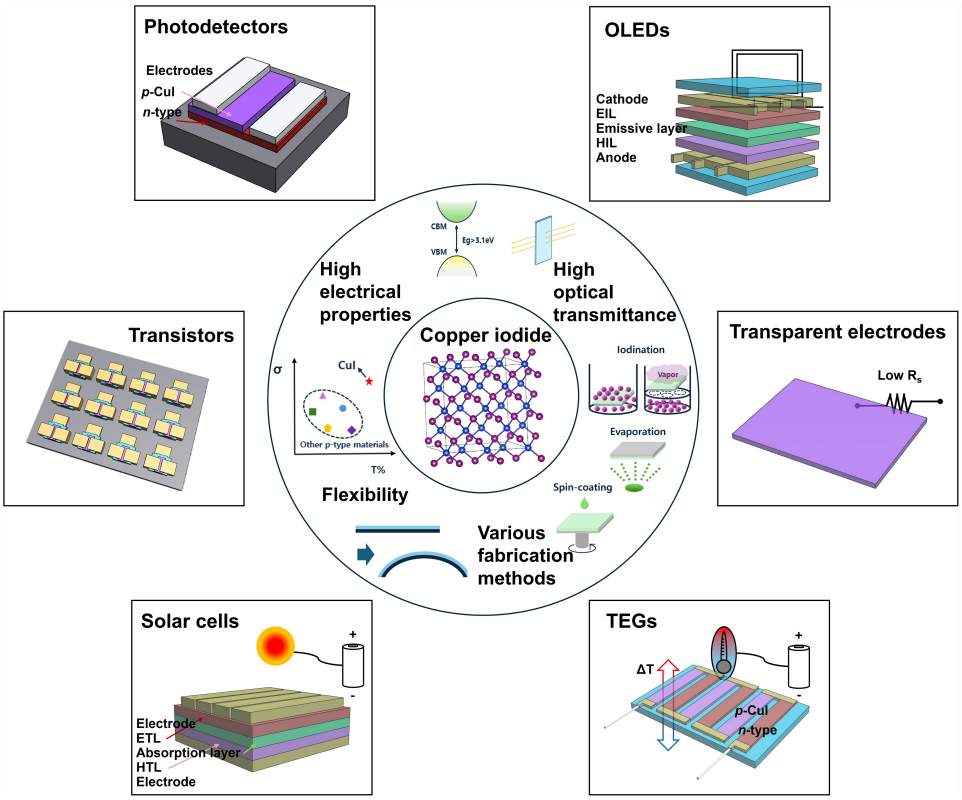

Figure 1. Intrinsic advantages of CuI and its various applications of CuI as a transparent and flexible *p*-type semiconductor for next-generation electronics devices. CuI: Copper iodide.

THEORETICAL ANALYSIS OF COPPER IODIDE

CuI exhibits various stable crystal structures including zinc-blende, wurtzite, tetragonal, and rock-salt structures, depending on the temperature and pressure. The γ-CuI adopted a zinc-blend structure below 643 K, and β-CuI, with a wurtzite structure, is stable between 643 and 673 K. Above 673 K, there exists the α-CuI with a rock-salt structure; with rising temperature, an anharmonic thermal vibration increases, enhancing ionic conductivity[50]. Kaindl *et al.* reported these phase transitions with different pressures at 4.2 K. The structural transition from γ-CuI to β-CuI, from α-CuI to a tetragonal phase, and from the tetragonal to α-CuI occurs at 18, 46, and 90 kbar, respectively. For γ-CuI, the hybridization between an iodine 5*p* orbital and a copper 3*d* orbital decreases with increasing pressure. Conversely, the hybridization increases with pressure for β-CuI and tetragonal phases[51].

The I 5*p*-Cu 3*d* orbital hybridization facilitates the movement of hole carriers by creating a more dispersed valance band and thus the delocalization of the electronic state within the band induces high μ_h. Moreover, the valance band of CuI is composed of heavy hole (hh) and light hole (lh) bands. Yu *et al.* reported the band structure of CuI and calculated a direct bandgap of 2.95 eV[52]. Figure 2A shows the energy levels of copper and halide orbitals within the bandgap, along with a diagram illustrating the interaction between Cu and I (halide) orbitals in the conduction and valence bands. The CBM is an antibonding state, composed of Cu 4*s* orbitals and I 5*p* orbitals. For the VBM, they also confirmed a strong hybridization[52]. Additionally, Tanaka *et al.* confirmed the energy separation of hh and lh. They measured the separation using photoluminescence due to a thermal deformation in different substrates[53]. Wang *et al.* reported computational results of the band structure of CuI and its intrinsic defects. They calculated the direct

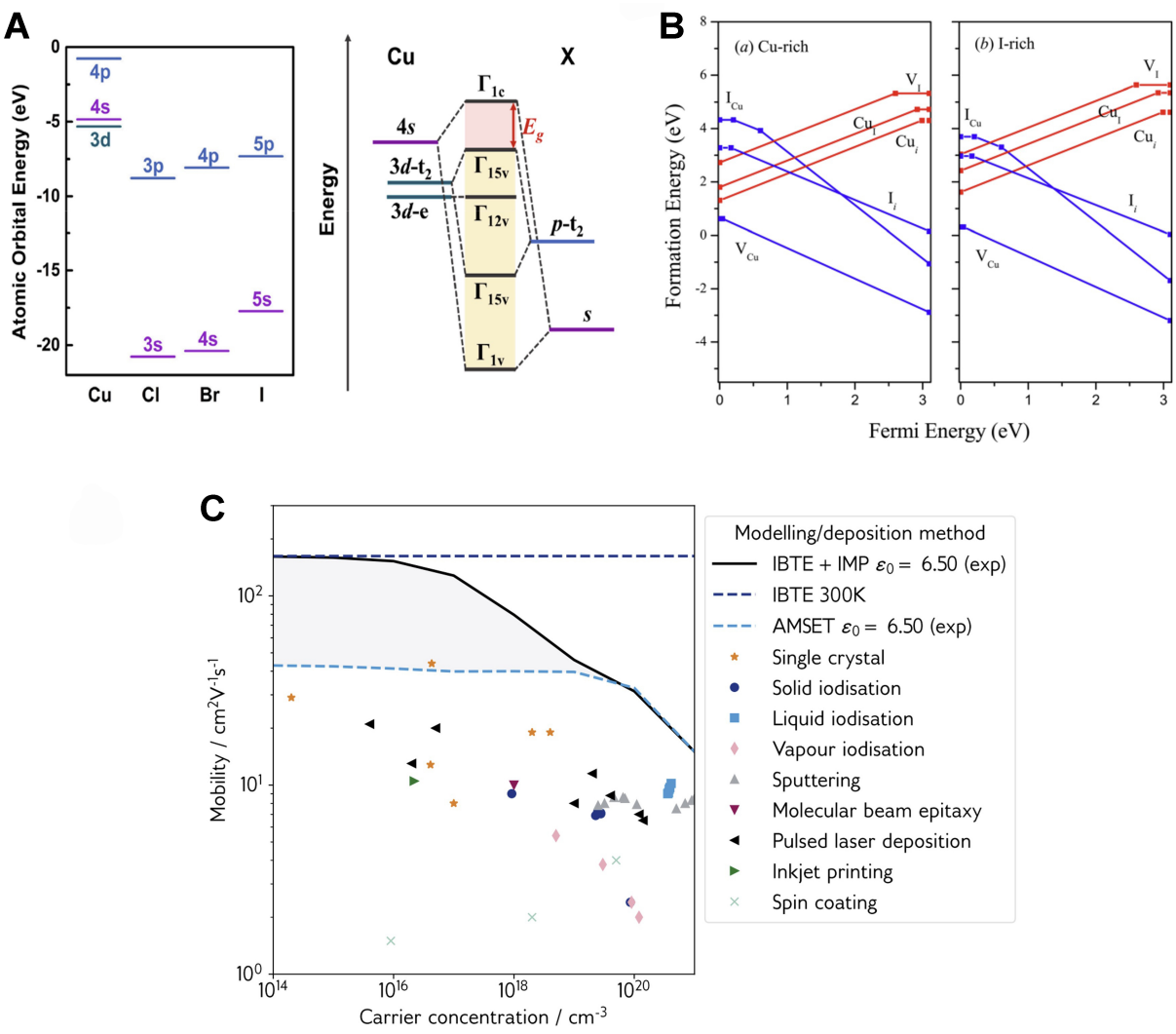

Figure 2. (A) Atomic orbital energy levels within the bandgap of copper halides and a diagram illustrating the interaction between Cu 4s orbitals and halide s orbitals in the conduction band, as well as Cu 3*d* orbitals and halide p orbitals[52]. Copyright 2024 Elsevier B.V.; (B) Formation energy of intrinsic defects in CuI[54]. Copyright 2024 AIP Publishing LLC; (C) Relationship between mobility and carrier concentration of CuI, based on experimental and computational data[14]. Copyright 2023 The Authors. Published by American Chemical Society.

bandgap of CuI as 3.1 eV. They also calculated the effective mass of hh and lh as 2.144 m_0 and 0.303 m_0, respectively. Moreover, they determined the formation energy of vacancies: Cu vacancy (V_{Cu}), I vacancy (V_I), Cu interstitial (Cu_i), I interstitial (I_i), Cu antisite (Cu_I), and I antisite (I_{Cu}) [Figure 2B]. Among these, V_{Cu} has the lowest formation energy. V_{Cu} acts as the intrinsic hole carrier of CuI, creating an acceptor level above the VBM[54].

Jaschik *et al.* investigated V_{Cu} more deeply, finding that defect complexes are stable at Cu_4I_5 and Cu_3I_4, with 20%-25% V_{Cu} defects. The total system energy decreases when V_{Cu} aligns with the [100] direction compared to isolated V_{Cu} states. As explained above, many copper and iodine vacancies are generated spontaneously in CuI, but other foreign elements can be used to control carrier concentrations and μ_h[55]. The most commonly reported dopants are iodine and O, which occupy anion vacancy sites. Iodine doping fills vacancy sites, increasing carrier concentrations because the iodine vacancy creates a donor level within the bandgap and

acts as compensation for the hole carrier. Darnige *et al.* reported various intrinsic defects in CuI, such as iodine and copper Frenkel and Schottky defects, noting that O can easily fill these defect sites when exposed to air[56]. Graužinytė *et al.* conducted a comprehensive study on CuI doping, examining 64 elements. They found S and Se to be promising *p*-type dopants that can significantly increase carrier concentration by replacing iodine sites. Although chalcogen impurities generally exhibit self-compensating behavior due to deep iodination energy, S and Se have low formation energy. In contrast, O, while easily doped on the surface, does not enhance carrier concentration effectively due to its high formation energy. For *n*-type doping, alkaline earth metals, group III and IV-B transition metals, tungsten, and most group VI-A elements were identified as potential candidates. However, due to the low formation energy of V_{Cu}, only beryllium and magnesium are suitable for *n*-type dopants. Despite these results, many *n*-type dopants such as Br, Zn, Ag, and Sn have been reported[30]. Yamada *et al.* calculated that $Cu_{1-x}Br_xI$ alloys can control carrier concentration from 10^{17} to 10^{20} cm^{-3} without significantly affecting transmittance and bandgap[57]. In 2023, Willis *et al.* reported the limitations of μ_h of CuI. They examined the phonon- and impurity-limited carrier mobility as a function of carrier concentration. The μ_h is limited to 162 $cm^2 \cdot V^{-1} \cdot s^{-1}$ in the phonon-limited region and 32.6 $cm^2 \cdot V^{-1} \cdot s^{-1}$ in the ionized impurity-limited region [Figure 2C]. In the high carrier concentration region, where degenerately doped conditions prevail, carrier mobility is dominated by ionized impurities. They also calculated that the intrinsic copper vacancy can lead to a carrier concentration of up to 2×10^{19} cm^{-3}. Moreover, they asserted that while S and Se can act as *p*-type dopants, those dopants may not directly affect the carrier concentration due to the high degree of charge localization and relatively high formation energy compared to V_{Cu}. They also mentioned the indirect effects of doping on the crystallinity and morphology of CuI, which may enhance its electrical properties[14].

ACTIVE LAYERS

Diode

CuI is well compatible with various *n*-type semiconductors, particularly metal oxides and metal halides such as ZnO, titanium oxide (TiO_2), silver iodide (AgI), and *a*-IGZO[58-61]. The *n*-ZnO/*p*-CuI heterojunction diode was reported by Schein *et al.* in 2013, which exhibited a current rectification ratio of 6×10^6 under ± 2 V and an ideality factor of $\eta = 2.14$[58]. In 2016, they further improved the *n*-ZnO/*p*-CuI heterojunction diode by using a heteroepitaxial method at room temperature, enhancing the film crystallinity. This device showed an improved rectification of up to 2×10^9 and a low saturation current density of 5×10^{-9} $A \cdot cm^{-2}$[59]. In 2021, Kim *et al.* reported an enhancement in rectification by incorporating a ZnS interfacial layer, which improved the rectification ratio from 2.38×10^2 to 1.71×10^7. As shown in Figure 3A, the ZnS interlayer enhances carrier transport between *n*-ZnO and *p*-CuI by lowering potential barriers and reducing O vacancy defects[62].

Lee *et al.* reported an *n*-$BaSnO_{3-\delta}$/*p*-CuI heterojunctions diode with a high rectification ratio of 6.75×10^5 under ± 2 V and an ideality factor of $\eta = 1.5$. The CuI layer was fabricated by thermal evaporation, which can generate iodine vacancy when the deposition process takes a long time for thick films. The increases in iodine vacancies and the decrease in built-in potential in the heterojunction led to an improved rectification ratio[63].

n-IGZO/*p*-CuI heterojunction diodes were reported by Yamada *et al.*, demonstrating a rectification ratio of 6×10^6 and an ideality factor of $\eta = 1.6$ [Figure 3B]. Polycrystalline CuI film was fabricated by solid-phase iodination of sputtered Cu_3N film under low temperatures[64]. The following year, the group reported an *n*-IGZO/*p*-$CuI_{1-x}Br_x$ heterojunction diode, controlling the composition of I and Br to adjust the hole density [Figure 3C][57]. A (111) oriented *p*-CuI film was grown by thermal evaporation, and an amorphous SiZnSnO (SZTO) film was grown using radio frequency (RF) magnetron sputtering method. The rectification ratio

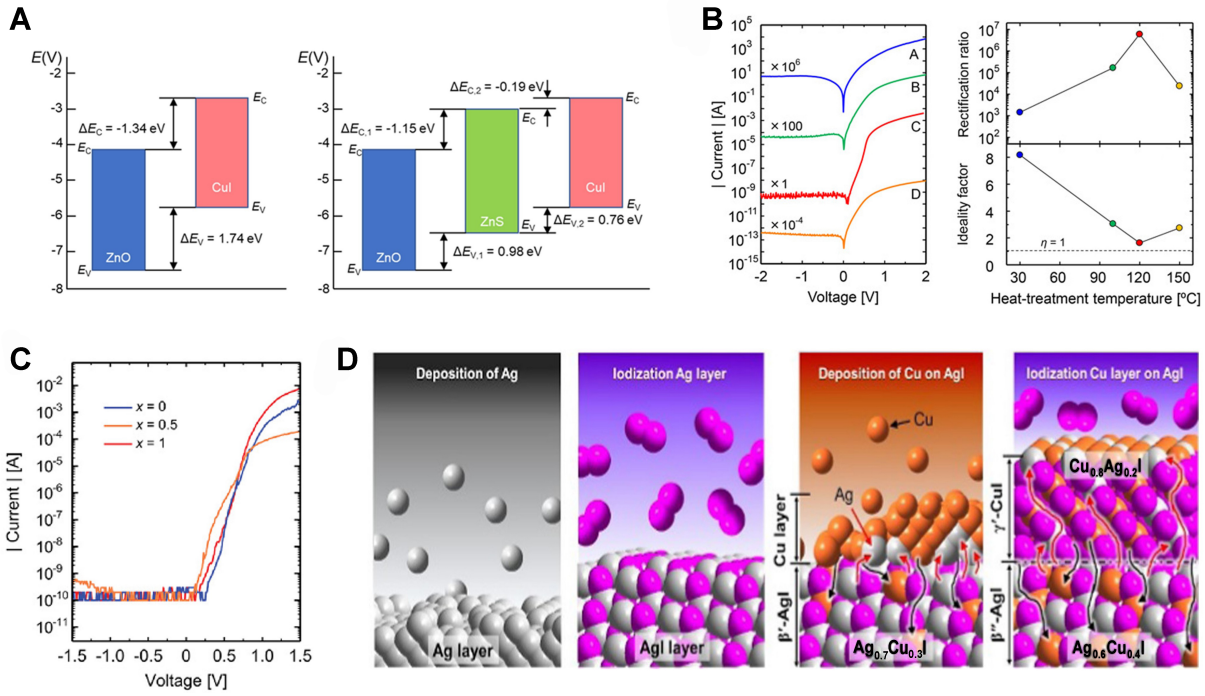

Figure 3. (A) Band alignment diagram of *n*-ZnO/*p*-CuI heterojunction diode with and without ZnS interface layer[62]. Copyright 2020 Elsevier B.V.; (B) Current-voltage (I-V) curves and ideal factor of the *n*-IGZO/*p*-CuI heterojunction diode under heat treatment at 100, 120, and 150 °C, labeled as B, C, and D, respectively (as-prepared sample is labeled A)[64]. Copyright 2018 WILEY-VCH Verlag GmbH & Co. KGaA, Weinheim; (C) I-V curve of *n*-IGZO/*p*-$CuI_{1-x}Br_x$ heterojunction diode according to the x[57]. Copyright 2020 WILEY-VCH Verlag GmbH & Co. KGaA, Weinheim; (D) Schematic illustration of the fabrication method of *n*-AgI/*p*-CuI heterojunction diode[61]. Copyright 2017, American Chemical Society. CuI: Copper iodide.

was enhanced to 10^7 by annealing the CuI film under a nitrogen atmosphere, which reduced ionized impurity scattering caused by V_{Cu} and the structural defects at the grain boundaries (GBs)[65]. This thermal annealing creates V_I, compensating for V_{Cu}. Furthermore, thermal energy facilitates the migration of V_{Cu} from the interior of the Cu film to the surface or GB, reducing ionized impurity scattering[64].

In addition to combinations with metal oxides, *n*-type metal halide semiconductors combined with *p*-CuI have also been reported[61]. In 2017, Cha *et al.* reported a transparent *n*-AgI/*p*-CuI heterojunction diode. They fabricated the diode through a two-step process of deposition of metal films and iodination [Figure 3D]. During this process, Cu diffused into the AgI layer, altering both the AgI and CuI layers near the interface. However, the CuI layer protected the AgI layer from decomposition, achieving air stability over 12 h and forming smooth and dense polycrystalline films, with a rectification ratio of 9.4×10^4[61]. Table 1 summarizes the properties of *p*-CuI/*n*-type semiconductor diodes.

TFT

For realization of transparent complementary circuits, high-performance transparent *p*-type channel layers are crucial for logic circuits as a counterpart to *n*-type metal oxide semiconductors[71-75]. Although many organic materials are reported as *p*-type transparent channel layers, more studies are needed to enhance their electrical performance and compatibility with other inorganic layers[76-79]. As described above, CuI is expected to be a suitable *p*-type semiconductor with high μ_h and excellent optical transmittance[38,66]. However, spontaneously generated excessive high levels of hole carriers up to 10^{19} cm^{-3} make the transistor performance of CuI poor, for instance, high off-current levels and low on/off current ratio. In 2016, the first CuI-based TFT was reported, fabricated by an inkjet printing method at a low temperature of 150 °C. It

Table 1. Summary of the characteristics of published data on CuI-based *p/n* diodes

p/n-diode	CuI fabrication method	Ideality factor η	Saturation current (A)	Rectification ratio IF/IR	Year[Ref.]
CuI/ZnO	Sputtering	1.7	1.3×10^{-11}	2×10^{7}, ± 2 V	2013[66]
CuI/ZnO	Vapor iodization of Cu film	1.6	6.2×10^{-15}	4×10^{7}, ± 2 V	2013[66]
CuI/ZnO	Thermal evaporation	1.8	3.2×10^{-13}	2×10^{7}, ± 2 V	2013[66]
CuI/ZnO	SILAR method	-	-	6×10^{2}, 3 V	2015[67]
CuI/ZnO	Epitaxial growth	1.7	1.1×10^{-12}	2×10^{9}, ± 2 V	2016[59]
CuI/$BaSnO_{3-\delta}$	Thermal evaporation	1.5	9.9×10^{-13}	7×10^{5}, ± 2 V	2017[63]
CuI/AgI	Vapor iodization of Cu film	1	-	9.4×10^{4}, ± 2 V	2017[61]
CuI/InGaZnO	Solid iodination of Cu_3N	1.6	-	6×10^{6}, ± 2 V	2018[64]
CuI/Ga_2O_3	Thermal evaporation	-	-	6×10^{3}, ± 2 V	2020[68]
$CuBr_{1-x}I_x$/InGaZnO	Thermal evaporation	1.9	2×10^{-12}	2×10^{9}, ± 1.5 V	2020[57]
CuI/ZnS/ZnO	Iodination of Cu film and spin-coating of CuI	1.1	-	1.7×10^{7}, ± 2 V	2021[62]
CuI/SiZnSnO	Thermal evaporation	2.7	0.7×10^{-16}	7×10^{7}, ± 2 V	2021[65]
CuI/TiO_2	Iodination of CuO film	4.4	-	-	2023[69]
CuI/ZnO	Iodination of CuN_3 film	1.22	-	1.05×10^{5}, ± 2 V	2024[70]

CuI: Copper iodide; IF: forward current; IR: reverse current; SILAR: successive ionic layer absorption and reaction.

exhibited an average field-effect mobility of 1.86 $cm^2 \cdot V^{-1} \cdot s^{-1}$ and an average on/off current ratio of 10^1 to 10^2. The inkjet printed CuI layer had a thickness of around 100 nm, although a thickness of a few tens of nanometers is preferable for reducing offset of threshold voltage and the off-current. However, when the thickness was reduced below 100 nm in that study, the resulting high surface roughness induced pores and discontinuous films[44]. In 2018, Liu *et al.* reported a room-temperature solution-processed CuI-based TFT. Thermal annealing accelerated the decomposition of iodine and facilitated the generation of vacancies, resulting in an increased presence of V_I. In addition, they revealed that when the thickness of the CuI layer was reduced to below 8 nm, the threshold voltage and on/off current ratio could be close to 0 V and over 10^2, respectively. This results in an enhanced on/off current ratio of 5×10^2 and mobility of 0.44 $cm^2 \cdot V^{-1} \cdot s^{-1}$[42].

To control carrier concentration, doping with *n*-type dopants, such as Zn, Ga, or Al as well as alloying, is an effective strategy[80]. A Zn-doped CuI-based TFT was fabricated using a solution process at a low annealing temperature of 80 °C. The 2.5% Zn-doped CuI-based TFT exhibited high electrical performance with a mobility of 5 $cm^2 \cdot V^{-1} \cdot s^{-1}$ and a high on/off current ratio of up to 10^7 at an optimal thickness of 9 nm, along with good operational stability and reproducibility [Figure 4A]. Zn doping reduces iodine vacancy generation and grain aggregation, improving its bias stability. This improvement originated from hole suppression and enhanced crystallinity with Zn^{2+} doping into CuI. In addition, the authors also investigated various metal cations (Ni^{2+}, Pb^{2+}, Bi^{3+}, Ga^{3+}, and Sn^{4+}) as dopants for CuI [Figure 4B]. CuI doped with 5 mol% of Bi^{3+} and Pb^{2+} exhibited mobility of 0.45 and 0.34 $cm^2 \cdot V^{-1} \cdot s^{-1}$, respectively, each with a similar on/off current ratio of 10^4. Given that the ionic radius of Pb^{2+} (120 pm) is larger than that of Bi^{3+} (108 pm), it is expected that the doping efficiency of Pb^{2+} would be lower than that of Bi^{3+}. Ga-doped CuI TFT exhibited poor performance, due to the small ionic radius, which can act as interstitial impurities. No transfer characteristics were achieved for Ni-doped TFT[80].

Br-doped CuI-based TFT was reported by Li *et al.*, fabricated by an inkjet printing method in 2022[81]. The inks consisted of a mixture of binary CuBr and CuI salts that formed crystalline $CuBr_xI_{1-x}$ alloys after printing and annealing at a low temperature of 60 °C. CuBr has a higher copper vacancy formation energy than CuI, which helps reduce carrier concentration. However, the mobility of CuBr is lower than that of CuI due to the narrower band dispersion of bromide 4*p* orbital in CuBr compared to the iodine 5*p* orbital in

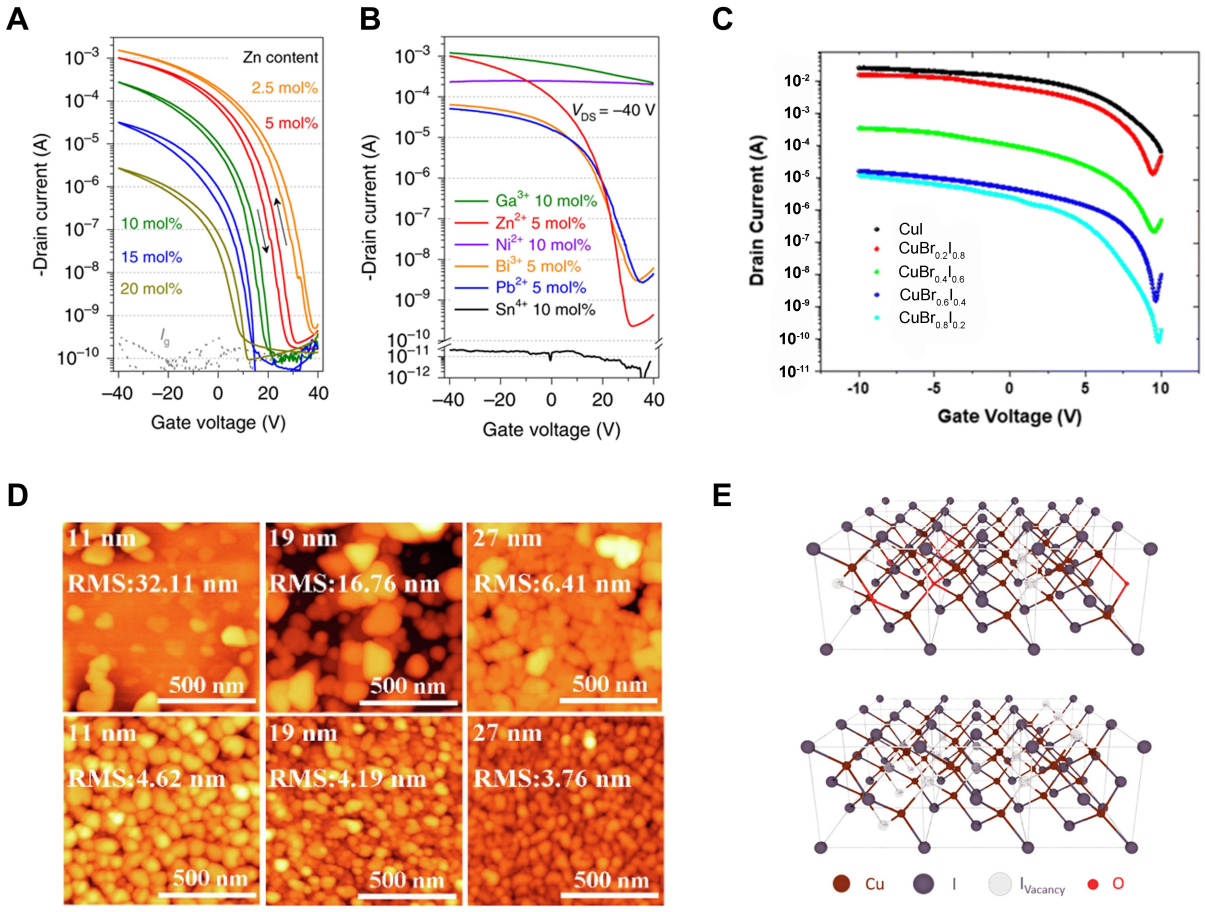

Figure 4. (A) Transfer characteristics of CuI-based TFT with various concentrations of Zn dopants[80]. Copyright 2020 The Authors. Published by Springer Nature; (B) Transfer characteristics of CuI-based TFT with various dopants (Ga^{3+}, Zn^{2+}, Ni^{2+}, Bi^{3+}, Pb^{2+}, and Sn^{4+}) at optimized concentrations[80]. Copyright 2020 The Authors. Published by Springer Nature; (C) Transfer curves of printed $CuBr_xI_{1-x}$ (x = 0, 0.2, 0.4, 0.6, and 0.8)-based TFTs[81]. Copyright 2022 The Royal Society of Chemistry; (D) Atomic force microscopy images of CuI surfaces on SiO_2/Si substrates (top layer) and CS films (bottom layer)[84]. Copyright 2022 Elsevier B.V.; (E) Schematics of the lattice structure of air-annealed and vacuum-annealed CuI[40]. Copyright 2022 American Chemical Society. CuI: Copper iodide; TFT: thin-film transistor.

CuI, resulting in smaller orbital overlap[39,57,82]. By increasing the ratio of Br compared to I in $CuBr_xI_{1-x}$, the on/off current ratio grew from 10^3 to 10^5, but the field effect mobility decreased from 9.06 to 0.02 $cm^2 \cdot V^{-1} \cdot s^{-1}$ [Figure 4C][81]. Another experiment about CuIBr-based TFT was reported in 2023 by Wei *et al.*; it was fabricated by a solution process at 100 °C under ambient conduction. The TFT demonstrated a high mobility of up to 5 $cm^2 \cdot V^{-1} \cdot s^{-1}$ and an on/off current ratio of up to 10^4 at 6.7% Br[83].

Recently, various strategies besides doping have been reported to improve the electrical properties of CuI-based TFTs[40,84,85]. Using high-capacitance dielectrics with mobile ions, such as ionic liquid, ion-gel, and solid electrolyte, is effective in reducing operation voltage and high current for low mobility-based TFT devices[86,87]. However, when calculating field-effect mobility with the device having high capacitance dielectrics with mobile ions, careful examination of mobility calculation is necessary. As reported by Liang *et al.*, ultrahigh-apparent mobility over ten times could be observed with synchronous ion motion in the dielectric layer[88]. Wu *et al.* reported CuI-based TFT constructed on a chitosan (CS) dielectric layer. The electrode and substrate were ITO and poly(ethylene terephthalate) (PET), respectively, for flexible TFT devices. This TFT demonstrated a high mobility of 65 $cm^2 \cdot V^{-1} \cdot s^{-1}$ and an on/off current ratio of 10^4. CS has a

high capacitance of over 0.5 μF·cm^{-2} and flexibility, making it suitable for high-performance flexible electronics. Moreover, the CuI-based TFT on CS with a curvature radius of 2 cm exhibited negligible current change compared to the unbent state. The high mobility of this TFT is attributed to the dense arrangement and fine grain size of CuI on the CS dielectric compared to the SiO_2 dielectric, formatting a smoother surface [Figure 4D]. Additionally, the smaller work function of CuI/CS films has a lower intrinsic hole concentration, contributing to the higher on/off current ratio[84]. Again, although there are various reports on high apparent mobility CuI-based TFT devices, it is crucial to note that the mobility of CuI in a single crystal was measured at 43.9 cm^2·V^{-1}·s^{-1}[32]. Considering the dielectric with mobile ions, such as ionic liquid, ion-gel, solid electrolyte or even poorly annealed inorganic dielectric with unintentional H^+, could result in unreliable field effect mobility estimation, it is always better to report field effect mobility with reliable dielectric layers, such as thermally grown SiO_2, atomic layer deposition (ALD) grown Al_2O_3, HfO_2 at high temperatures.

In 2022, Lee *et al.* reported the effect of ALD grown Al_2O_3 capping layers to passivate solution-processed CuI-based TFT. As shown in Figure 4E, annealing under a vacuum atmosphere increased V_I, enhancing carrier mobility and reducing carrier concentration. Furthermore, annealing in vacuum improved film density and reduced voids, enhancing crystallinity and electrical properties. Through the synergistic effect of V_I generation due to trimethylaluminum (TMA, AlC_3H_9) used to deposit the Al_2O_3 passivation layer, TMA reduces Cu in the CuI thin film, leading to an increase in V_I. As a result, the TFT device exhibited a field effect mobility of 4.02 cm^2·V^{-1}·s^{-1} and an on/off current ratio of 1.12 × 10^4[40]. In 2024, the same group reported CuI-based TFT fabrication with the CuI channel layer sandwiched structure between both interfacial and passivation Al_2O_3 layers, achieving a mobility of 6.54 cm^2·V^{-1}·s^{-1} and an on/off current ratio of 1.01 × 10^5. By capping the CuI channel with an Al_2O_3 passivation layer, which was deposited by ALD process, hydrogen in the capping layer diffused into the channel layer and generated V_I, reducing hole concentration. Furthermore, the crystallinity and surface morphology of the thin film on the interfacial Al_2O_3 were improved, resulting in increased mobility[85]. The properties of CuI-based TFTs are summarized in Table 2.

Photodetector

CuI was used as an ultraviolet (UV) light photodetector with flexibility and transparency similar to organic photodetectors[64,92-96]. Furthermore, the wide bandgap of CuI helps in reducing the dark current, which flows through the photodetectors in the absence of light, thereby enhancing the signal-to-noise ratio[97]. Typically, photodetectors have *p*/*n* heterostructure, metal-semiconductor-metal (MSM) structures, and so on[98]. Here, we investigate CuI-based photodetectors with heterostructures or MSM structures, and the properties of these photodetectors are presented.

In 2022, Huang *et al.* reported a CuI-based self-powered 365 nm UV photodetector. With an MSM structure and silver electrode, the CuI layer was fabricated by solid iodination on a polyimide (PI) substrate. The device exhibits optical switching behavior under alternating light (rise time of 21.1 s and decay time of 23.3 s under 1 V). The average transmittance at visible region (400 to 800 nm) was 90%[92]. Tasy *et al.* also fabricated an MSM structure with Ni- and Zn-doped CuI layers. The Zn-doped CuI layer was fabricated by the solution process. The Zn substitution improves the crystallinity and increases the grain size, decreasing resistivity and increasing mobility. Consequently, the Zn-doped CuI photodetector exhibits optimal performance with a response current of 2.05 × 10^{-4} A, responsivity of 722 mA·W^{-1}, and specific detectivity of 1.51 × 10^8 Jones. The external quantum efficiency (EQE) also enhanced from 62.2% in the undoped device to 242% in the 8% Zn-doped device[93].

Table 2. Summary of the characteristics of published data on CuI-based TFTs

Channel/dielectric	Fabrication method	Annealing temp. (°C)	V_{DS} (V)	Mobility ($cm^2 \cdot V^{-1} \cdot s^{-1}$)	I_{on}/I_{off}	Year[Ref.]
CuI/SiO_2	Ink-jet	60	-40	1.86 ± 1.6 (max 4.4)	10^1-10^2	2016[44]
CuI/SiO_2	Spin-coating	RT	-50	0.44	5×10^2	2018[42]
CuI/ZrO_2	Spin-coating	-	-1, -5	1.93	10^2	2018[42]
CuI/SiO_2	Magnetron sputtering	140	-1	4.8	10^2	2019[89]
Zn-CuI/SiO_2	Spin-coating	80	-40	5.3 ± 0.5	10^6-10^7	2020[80]
Zn-CuI/SiO_2	Spin-coating (O_2 treated)	80	-40	4.4	8×10^6	2021[90]
$CuBr_xI_{1-x}/SiO_2$	Ink-jet	150	-1, -10	0.02-9.06	10^3-10^5	2022[81]
Al_2O_3/CuI/SiO_2	Spin-coating	300 (vacuum)	-5	4.02	1.12×10^4	2022[40]
Su8/CuBrI/SiO_2 + Al_2O_3	Spin-coating	100	-1	5	10^4	2023[83]
Zn-CuI/SiO_2	Spin-coating APTES SAM treatment	120	-30	1.24	1.1×10^7	2023[91]
CuI/CS	Spin-coating	RT	-1	60	6.6×10^3	2023[84]

CuI: Copper iodide; TFTs: thin-film transistors; RT: room temperature; APTES: (3-aminopropyl)triethoxysilane; SAM: self-assembled monolayer; CS: chitosan.

Yamada *et al.* reported a photovoltaic effect in *a*-IGZO and CuI under UV light. The high Hall mobility of CuI, around 20 $cm^2 \cdot V^{-1} \cdot s^{-1}$, resulted in good rectification performance with a-IGZO. Figure 5A shows the current-voltage (I-V) curve under dark and light conditions, under 365 nm UV illumination[64]. The same year, the author reported a heterojunction structure with *a*-IGZO and CuI for a self-powered UV photodetector. The device has a responsivity of 0.6 $mA \cdot W^{-1}$, detectivity of 8.4×10^{11} Jones, a rise time of 2.5 ms, and a decay time of 35 ms [Figure 5B and C][94].

Cao *et al.* reported a self-powered *n*-ZnO/*p*-CuI heterojunction photodetector with Au nanoparticles. The *n*-ZnO and *p*-CuI layers were fabricated using plasma-enhanced ALD (PEALD) and a solid-iodination method, respectively, with Au nanoparticles added by ion plating on the CuI film [Figure 5D]. The device exhibited high performance with a responsivity of 61.5 $mA \cdot W^{-1}$, detectivity of 1.7×10^{10} Jones, and rise and decay times of 0.41 and 0.08 s, respectively [Figure 5E and F][96]. In 2023, Shyam *et al.* applied ZnS shells between ZnO nanorods and a CuI thin film, improving charge separation and reducing recombination. Figure 5G and H show the improved optoelectrical performances of the *p*-CuI/ZnS/*n*-ZnO nanorod photodetector, with responsivity increasing from 25.11 to 43.85 $mA \cdot W^{-1}$, detectivity from 4.59×10^{13} to 3.84×10^{14} Jones, and rise and decay times changing from 211 to 305 ms and from 220 to 261 ms, respectively, compared to the *p*-CuI/*n*-ZnO heterojunction photodetector. The ZnS intermediate layer between the *p*-CuI and *n*-ZnO nanorod reduced the band offsets and hence effectively improved carrier transport [Figure 5I][99].

In 2019, Madusanka *et al.* reported a self-powered *n*-Cu_2O/*p*-CuI heterojunction-based UV-visible photodetector. The *n*-Cu_2O film was prepared on Cu plates through an atmospheric pressure hydrothermal method using a $CuSO_4$ solution, and the CuI film was deposited on *n*-Cu_2O by the drop-cast method. The *n*-Cu_2O/*p*-CuI heterojunction-based photodetector exhibited a high sensitivity of 2.355×10^5 for visible light and 7×10^3 for UV light at zero bias. In addition, responsivity was 250 $mA \cdot W^{-1}$ and rise and decay times were 582 and 817 μs, respectively[100]. Zhou *et al.* reported a self-powered UV photodetector based on a *n*-GaN/*p*-CuI heterojunction. The device was fabricated by depositing high-quality [111] orientation-preferred CuI thin film on GaN epilayers using vacuum thermal evaporation. The photodetector exhibited good optoelectrical properties, including a responsivity of 75.5 $mA \cdot W^{-1}$, a specific detectivity of 1.27×10^{12} Jones, and an on/off ratio of approximately 2,320 at 0 V under 360 nm UV illumination, with fast response and recovery times of 160 and 158 ms, respectively. Moreover, the atmosphere stability was also impressive

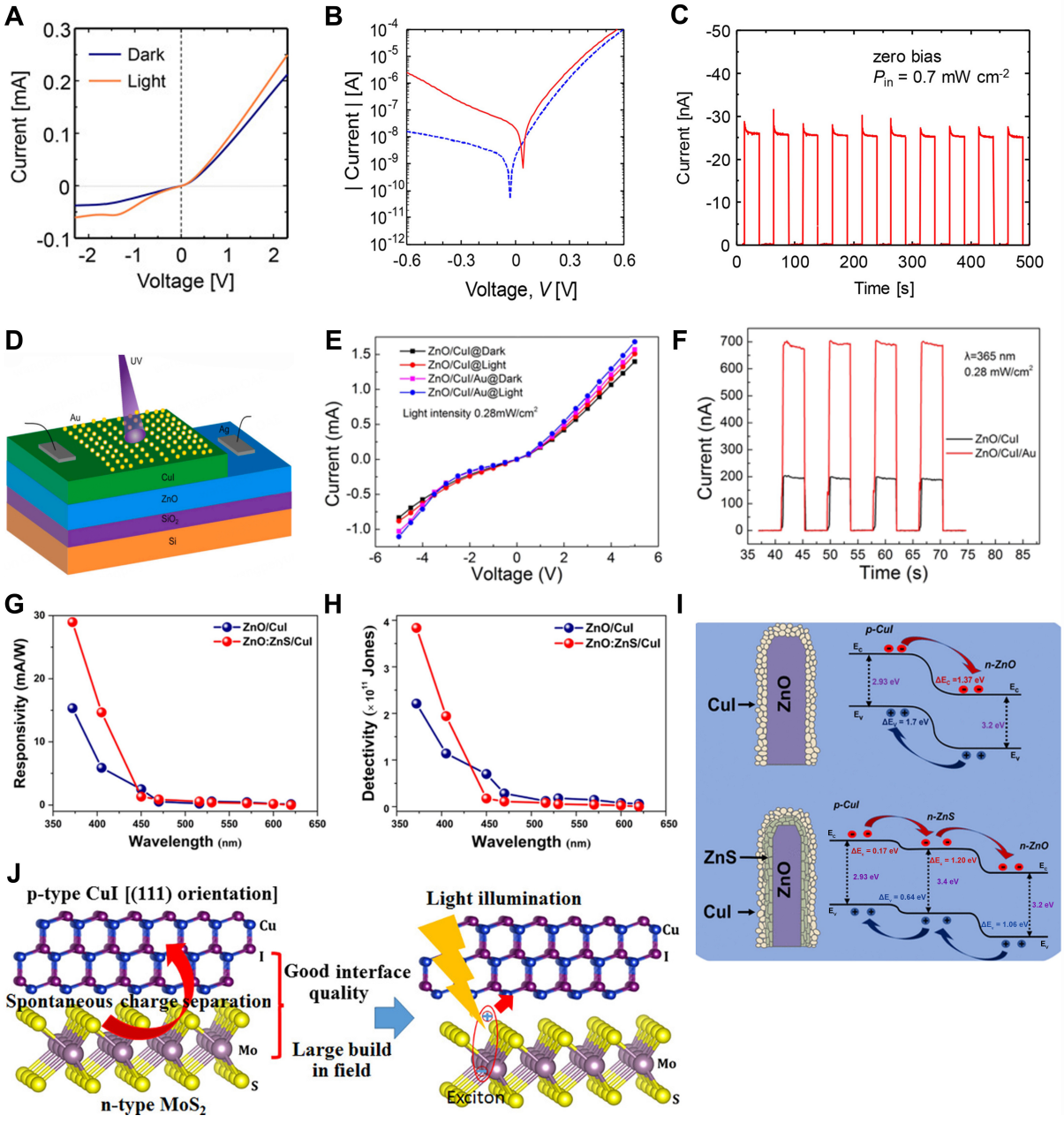

Figure 5. (A) I-V curves of the CuI/IGZO/ITO/glass device under dark and light conditions[64]. Copyright 2018 WILEY-VCH Verlag GmbH & Co. KGaA, Weinheim; (B) I-V curves of CuI/*a*-IGZO device[94]. Copyright 2019 Elsevier Ltd.; (C) Time-dependent photoresponse of the CuI/*a*-GIZO device under the alternating on/off cycles of UV illumination[94]. Copyright 2019 Elsevier Ltd.; (D) Structure of ZnO/CuI/Au device[96]; (E) I-V curves and (F) time-dependent photoresponse of the ZnO/CuI and ZnO/CuI/Au structures. Copyright 2020 Elsevier B.V.; (G) Wavelength-dependent spectral responsivity; (H) detectivity and (I) band diagrams of CuI/ZnO and CuI/ZnS/ZnO structures[99]. Copyright 2023 American Chemical Society; (J) Schematics of the formation of an effective interface for exciton dissociation and separation[102]. Copyright 2019 American Chemical Society. CuI: Copper iodide; IGZO: In-Ga-Zn-O; ITO: Sn-doped In_2O_3.

with similar photoresponse performance after 100 days[101].

Mahyavanshi *et al.* reported a photoresponsive device based on a *p*-CuI/*n*-MoS_2 heterojunction, exhibiting high photoresponsivity of 0.27 A·W^{-1} at a bias voltage of 5 V, which is comparable to commercial or other

photodiodes. The photoluminescence quenching effect and the formation of an effective interface between CuI and MoS_2 facilitated efficient exciton dissociation and charge separation, thereby enhancing the optoelectronic performance [Figure 5J][102]. Zhang *et al.* reported a self-powered UV photodetector utilizing a *p*-CuI/*n*-$CsPbBr_3$ heterojunction, which exhibited a high photocurrent of nearly 100 nA, high photosensitivity with an on/off ratio of 1.5×10^3, excellent wavelength selectivity between 565-525 nm, and a fast response speed with rise and decay times of 0.04 and 2.96 ms at 540 nm under zero bias. These results indicate that the CuI layer can form a good interface and achieves excellent optoelectronic performance, combined with various kinds of *n*-type materials[103]. Table 3 indicates the properties of published data of CuI-based photodetectors.

TRANSPARENT CONDUCTIVE ELECTRODES

Transparent conductive electrode

As a TCE, CuI has been reported to have a record-high electrical conductivity of 596 $S \cdot cm^{-1}$, with over 80% transmittance in the visible region[28]. Consistent with computational reports, sulfur and selenium doping is promising for enhancing carrier concentration, although further studies are needed. In intrinsic CuI without any dopant atoms, a record-high electrical conductivity of 283 $S \cdot cm^{-1}$ has been achieved with temporal iodine doping at the film surface[38]. To enhance mobility, decreasing defects through annealing or doping is an effective strategy. Here, we explore various methods to enhance electrical and optical properties, such as doping, fabrication methods, and encapsulation, which guide future efforts to further improve electrical conductivity.

Sulfur-doped CuI has been reported to exhibit the highest electrical conductivity with high optical transmittance. In 2022, Ahn *et al.* reported that sulfur-doped CuI had a high electrical conductivity of 511 $S \cdot cm^{-1}$ (carrier concentration of 3.2×10^{20} cm^{-3} and mobility of 9.8 $cm^2 \cdot V^{-1} \cdot s^{-1}$) and a high transmittance of over 80%. Moreover, with O doping by hydrogen peroxide treatment on the surface of the CuI thin film, the electrical conductivity increased to 596 $S \cdot cm^{-1}$ without any change in transmittance. The fabrication method for sulfur-doped CuI was liquid iodination, and computational experiments confirmed that this method has a lower doping formation energy compared to vapor iodination [Figure 6A]. The CuI thin film also underwent a bending test, bending 1,000 times with a 2 cm radius, showing a resistivity increase of only 2.6% compared to before bending. Additionally, it was applied as a source/drain electrode, demonstrating a fully transparent TFT, and as an anode electrode layer for organic light emitting diodes (OLEDs)[28]. In 2023, Mirza *et al.* reported sulfur-doped CuI using the PLD method. The CuI film exhibited a high carrier concentration of up to 9×10^{20} cm^{-3} and a high electrical conductivity of 435 $S \cdot cm^{-1}$. The transmittance was over 75%. They confirmed that the doped sulfur forms amorphous Cu_xS phases at GBs in CuI thin films[46]. In 2024, Son *et al.* reported on sulfur-doped CuI using solution processes with thiourea derivatives. N-ethylthiourea was identified as an optimal dopant, allowing control of the carrier concentration from 9×10^{18} to 2.52×10^{20} cm^{-3}, and achieving a conductivity of 390.7 $S \cdot cm^{-1}$[34].

Selenium-doped CuI on *c*-sapphire substrates was reported by Storm *et al.* in 2023. The selenium content varied from 0.1 at.% to 10 at.%. They confirmed that when the selenium content is higher than 1 at.%, the phase was changed due to selenium doping at iodine sites, leading to lower transmittance and electrical conductivity. With less than 1 at.% of Se, the carrier concentration increased from 10^{15} to 8×10^{17} cm^{-3}. However, with selenium content between 1 at.% to 3 at.% in CuI, the carrier concentration decreased to 10^{16} cm^{-3} and then increased again to 8×10^{17} cm^{-3} up to 10 at.% Se [Figure 6B]. The hole mobility reached 21 $cm^2 \cdot V^{-1} \cdot s^{-1}$ at around 1 at.% Se doping (carrier concentration of 8×10^{17} cm^{-3}). The transmittance also remained over 80% up to 1 at.% Se-doped CuI[109].

Table 3. Summary of the characteristics of published data on CuI-based photodetectors

p/n heterojunction	Fabrication method	Wavelength (nm)	Bias (V)	Responsivity ($mA \cdot W^{-1}$)	Detectivity (Jones)	Rise time (s)	Decay time (s)	Year[Ref.]
CuI/a-IGZO	Solid iodination of Cu_3N film	365	0	0.3	-	-	-	2018[64]
CuI/Si	Hydrothermal method	365	0	1.26	-	-	-	2019[104]
CuI/$CsPbBr_3$	Immersion process	540	0	1.4	6.2×10^{10}	4×10^{-5}	2.96×10^{-2}	2019[103]
Sn-CuI/ZnO	Spin coating	350	5	2.62	3.23×10^{11}	19.61	2.65	2019[95]
CuI/a-IGZO	Solid iodination of Cu_3N film	365	0	0.6	-	2.5×10^{-3}	3.5×10^{-2}	2019[94]
CuI/Cu_2O	Drop cast method	365	0	250	6.91×10^{10}	5.82×10^{-4}	8.17×10^{-4}	2019[100]
CuI/ZnO	Thermal evaporation	385	-5	235	1.23×10^{12}	-	-	2020[105]
CuI/ZnO	Iodination of Cu film	365	0	17.7	5×10^{9}	0.41	0.24	2021[96]
Au/CuI/ZnO	Solid iodination of Cu film	365	0	61.5	1.7×10^{10}	0.41	0.08	2021[96]
CuI	Spin coating	Blue light	1	45.64	6.53×10^{9}	7	7.5	2021[106]
CuI/Si	Spin coating	500	3	65.16	1.66×10^{10}	3	4.5	2021[107]
CuI/TiO_2	Thermal evaporation	310	0	0.67	8.4×10^{11}	1.1×10^{-4}	7.2×10^{-4}	2021[60]
CuI/GaN	Thermal evaporation	360	0	75.5	1.27×10^{12}	-	-	2022[101]
CuI	Solid iodination of Cu film	365	1	-	-	21.2	23.3	2022[92]
CuI/n-Si	Solid iodination of Cu film	365	0	123.3	5.7×10^{12}	9×10^{-5}	1.4×10^{-4}	2022[92]
Zn-CuI	Spin coating	UVA	0.5	722	1.51×10^{8}	-	-	2022[93]
CuI/ZnO nanorod	Spin coating	372	0	25.11	2.21×10^{12}	0.211	0.22	2023[99]
CuI/ZnS/ZnO nanorod	Spin coating	372	0	43.85	3.84×10^{14}	0.305	0.261	2023[99]
CuI/$ZnGa_2O_4$	Thermal evaporation	260	0	2.75	1.10×10^{11}	0.205	0.133	2024[108]

CuI: Copper iodide; IGZO: In-Ga-Zn-O.

Unlike chalcogen doping such as sulfur and selenium, excess iodine doping is a more traditional method to enhance electrical conductivity. In 2016, Yang *et al.* reported sputtered CuI using a mixed gas of iodine and argon. The high iodine concentration during deposition resulted in CuI thin films with low V_I, which created a donor level inside the bandgap. With additional surface iodine doping, CuI deposition in an iodine-rich environment had an electrical conductivity of 283 $S \cdot cm^{-1}$[38].

Alkali metal impurities for enhancing the *p*-type conductivity of CuI were reported by Matsuzaki *et al.* in 2022. The size mismatch between Cs^+ and Cu^+ in the host lattice allows for interstitial positions, making stable impurity-defect complexes [Figure 6C]. The Cs^+ impurity enhances hole concentration control from 10^{13} to 10^{19} cm^{-3}, with mobility increasing from 1 to 4 $cm^2 \cdot V^{-1} \cdot s^{-1}$. They also conducted calculations showing that the Cs^+ impurity forms impurity-defect complexes, which create shallow acceptor levels in the bandgap. The Coulomb repulsion between the moderately large size alkali metal impurity and the nearest neighboring Cu enhances the formation of acceptor-type V_{Cu} defects[110].

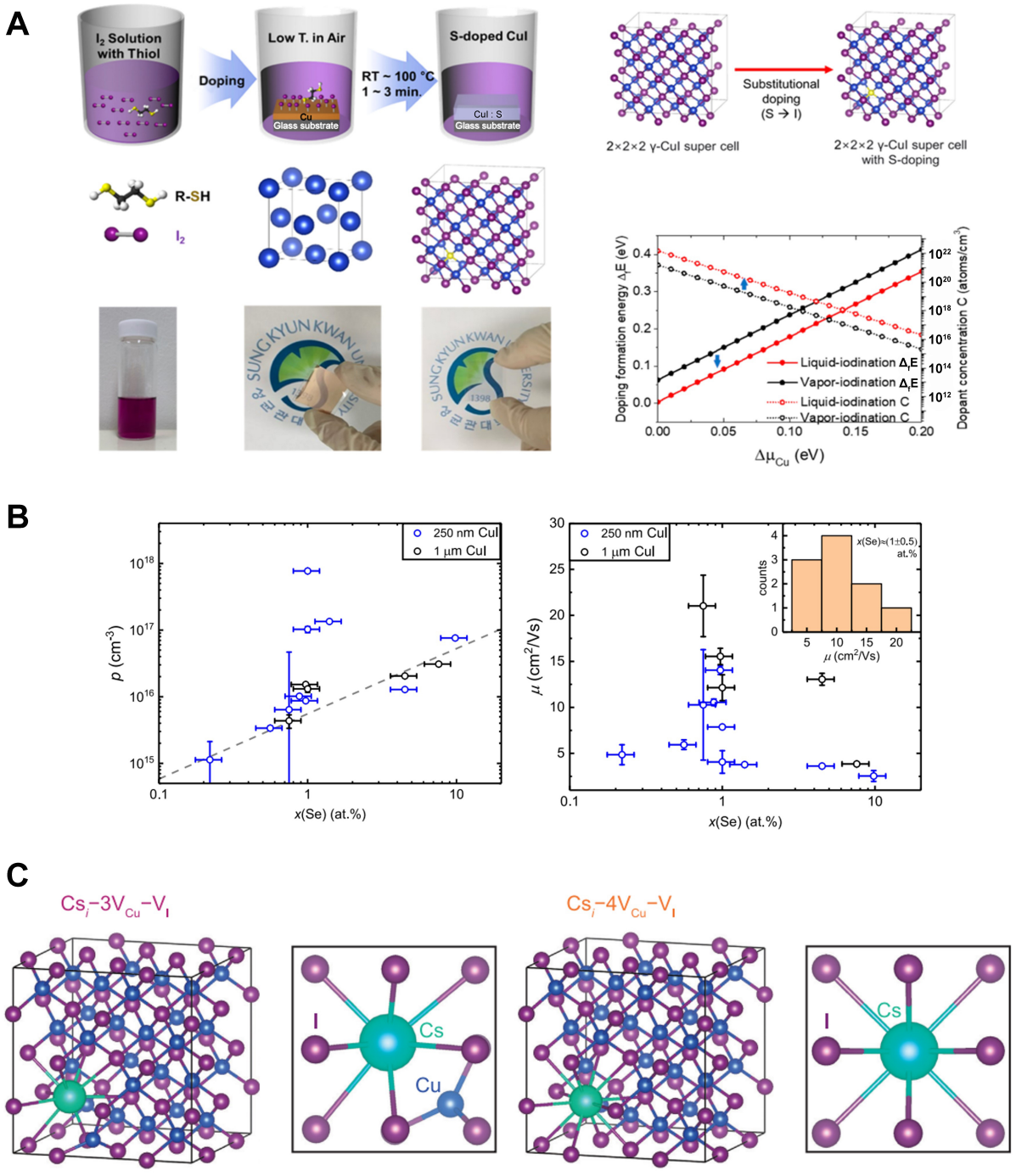

Figure 6. (A) (left) Fabrication method for sulfur-doped iodination, including photographs of the Cu and CuI thin films. (right) DFT calculation of doping formation energy and doping concentration of sulfur during vapor and liquid iodination[28]. Copyright 2022 American Chemical Society; (B) Hole carrier concentration and mobility of selenium-doped CuI films[109]. Copyright 2021 John Wiley & Sons, Inc; (C) Defect complex structure of Cs-doped CuI thin film[110]. Copyright 2022 American Chemical Society. CuI: Copper iodide; DFT: density functional theory.

CuI with a TiO_2 layer, made by co-depositing Cu with TiO_2 followed by iodination, increasing electrical conductivity and stability, was reported by Raj *et al.* in 2019. A high conductive space-charge layer was formed at the CuI-TiO_2 interface. The carrier concentration increased from 4×10^{19} to 1.3×10^{20} cm^{-3}, and

mobility slightly grew from 2.75 to 3.5 $cm^2 \cdot V^{-1} \cdot s^{-1}$. Moreover, TiO_2 suppressed recrystallization and grain growth in CuI, and also suppressed iodine loss and oxidation of CuI. The resistivity of CuI without TiO_2 was 56 mΩ cm (approximately 18 $S \cdot cm^{-1}$), whereas that of CuI with TiO_2 was 14 mΩ cm (approximately 71 $S \cdot cm^{-1}$). Additionally, the stability over six months in the air was impressively enhanced with the introduction of TiO_2. The resistivity and transmittance of CuI without TiO_2 increased more than four times and decreased to below 50%, respectively. However, the resistivity changed only by 5% and the transmittance was maintained in the presence of TiO_2[111]. Xue *et al.* fabricated CuI-Cu_2O thin films in 2023. The surface morphology and electronic properties were enhanced with Cu_2O because Cu_2O suppressed the migration through CuI GBs during iodination, reducing grain size. They controlled the O flow during Cu deposition using sputtering. Under optimized conditions, the CuI-Cu_2O had a carrier concentration of 6.16×10^{18} cm^{-3}, hole mobility of 25.4 $cm^2 \cdot V^{-1} \cdot s^{-1}$, and electrical conductivity of 18.57 $S \cdot cm^{-1}$. Regarding stability in ambient conditions over six months, the electrical conductivity of CuI without Cu_2O decreased by 53%, whereas that of CuI with Cu_2O decreased by 32%[112].

Inagaki *et al.* reported a high-quality CuI thin film on an Al_2O_3 substrate in 2020. They adopted a 2 nm CuI buffer layer to achieve high crystalline and low defect CuI layers. A relatively low deposition temperature (160 °C) for the buffer layer was effective in mitigating defects. The electrical conductivity ranged from 0.1 to 1 $S \cdot cm^{-1}$, the carrier concentration increased from 10^{17} to 10^{18} cm^{-3}, and mobility increased from 1-5 to 10 $cm^2 \cdot V^{-1} \cdot s^{-1}$ after adopting the buffer layer[113].

In addition to research into doping, many studies on CuI using different fabrication methods have been reported. These CuI films generally exhibit good transmittance around 80% and flexible properties. CuI thin films have been made by thermal evaporation, solution processing, PLD, sputter, iodination methods, and more. The PLD process can introduce various dopants during deposition, and the sputtering process is also conducive to doping by adding gas during iodination. In the case of iodination, solid-iodinated CuI films showed higher transmittance than the vapor-iodinated ones. Most of the results mentioned above are summarized in Figure 7[28,32,34,36-39,46,109-118]. The colored lines represent the electrical conductivity according to the carrier concentration and mobility. The electrical conductivity was calculated using $\sigma = n \cdot e \cdot \mu$, where the σ, n, e, and μ are electrical conductivity, carrier concentration, the charge of an electron (1.602×10^{-19} C), and mobility, respectively. When the electrical conductivity exceeds 1,000 $S \cdot cm^{-1}$, CuI can be compatible with *n*-type TCEs such as ITO. S-doped or I-rich CuI thin films can exceed the 100 $S \cdot cm^{-1}$ line. To achieve industrially viable optoelectrical performance of CuI, further innovations are needed for effective doping and high carrier mobility. Additionally, we compared the electrical conductivity and transmittance of CuI films across different fabrication methods. Regardless of the method, CuI films generally exhibit optical transmittance of around 80% in the visible region. However, the CuI films from liquid iodination and PLD methods with chalcogen doping demonstrate superior electrical conductivity [Figure 8]. The electrical conductivity result corresponds with the result in Figure 7.

For further enhancement of the conductivity of CuI, it is crucial to overcome trade-off between hole concentration and hole mobility or even to achieve synergetic improvement in both. In 2020, Crovetto *et al.* reported on the hygroscopic nature of CuI under ambient humidity. The electrical conductivity doubled when exposed to ambient humidity for 5 h, and the work function decreased by 1 eV. This is because hydration at the GB may be beneficial for overall hole mobility[114]. In 2023, Stralka *et al.* reported on the conductive properties of grains and GBs in CuI using current probe force microscopy (cp-AFM). They measured current densities across voltage ranges, finding that current primarily flows through GBs at low voltages. Above that voltage (roughly 50 to 100 mV), current begins to flow through the grain surface as well. However, the grain surface is susceptible to oxidation under ambient conditions, which causes surface

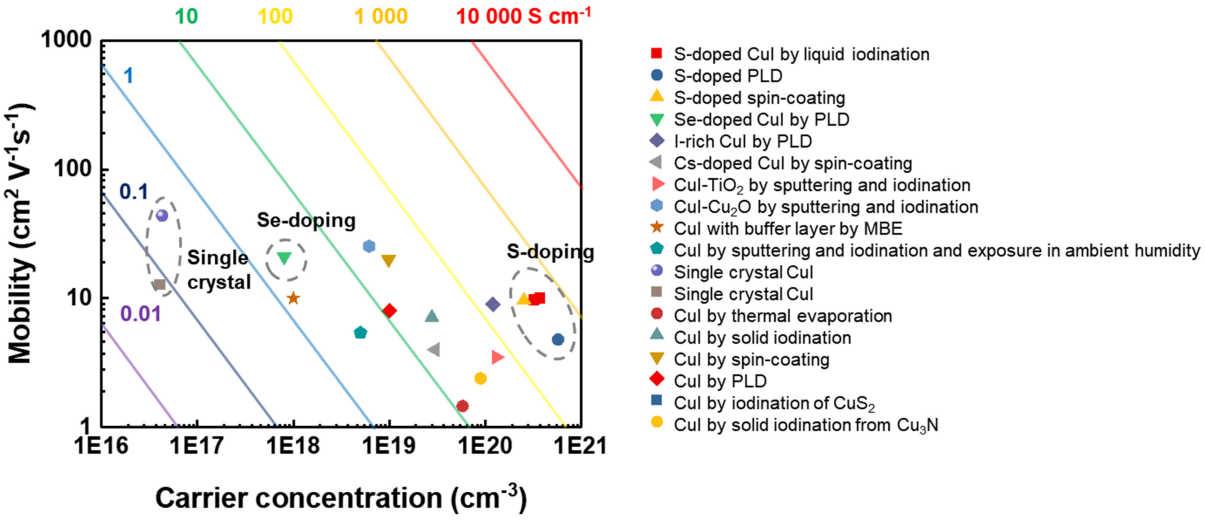

Figure 7. Summary of published data on CuI, categorized by carrier concentration and mobility. The electrical conductivity is indicated by the colored lines. References for each experiment from top to bottom: [28,46,34,109,38,110,111,112,113,114,32,115,36,116,117,37,118,39]. CuI: Copper iodide.

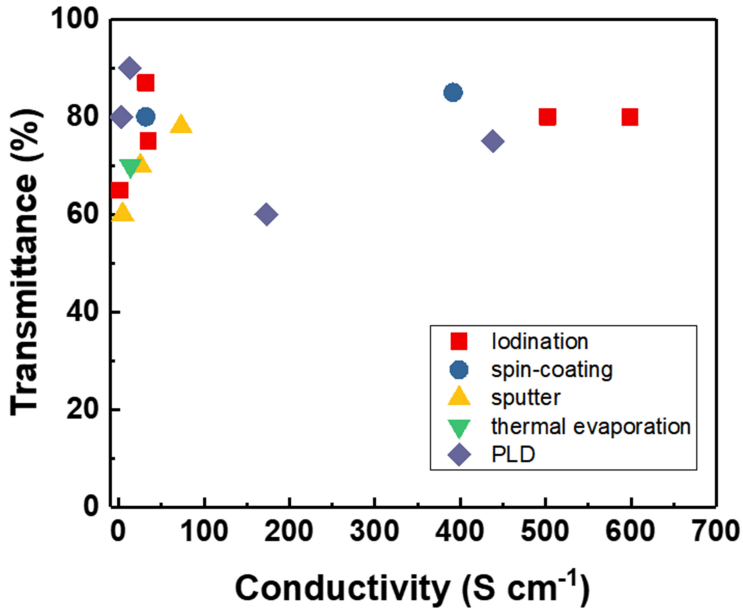

Figure 8. Summary of published data on CuI, comparing transmittance and electrical conductivity across different fabrication methods[28,34,36-39,46,109,111,112,114,116-118]. CuI: Copper iodide.

conductivity to decrease over time, while the GBs maintained their conductivity for longer periods [Figure 9A][119]. Another important study is on the single crystal of CuI. In 2020, Chen *et al.* attempted to produce high-quality single crystal CuI and obtained a large crystal with dimensions of 15 mm × 10 mm × 1 mm. The photograph of the single crystal is in Figure 9B. This crystal exhibited a mobility of 43.9 $cm^2 \cdot V^{-1} \cdot s^{-1}$[32]. In 2015, Lv *et al.* also reported single crystalline CuI with a resistivity of 11.97 Ω cm (0.08 $S \cdot cm^{-1}$), mobility of 12.81 $cm^2 \cdot V^{-1} \cdot s^{-1}$, and a carrier concentration of 4.08×10^{16} cm^{-3}[115].

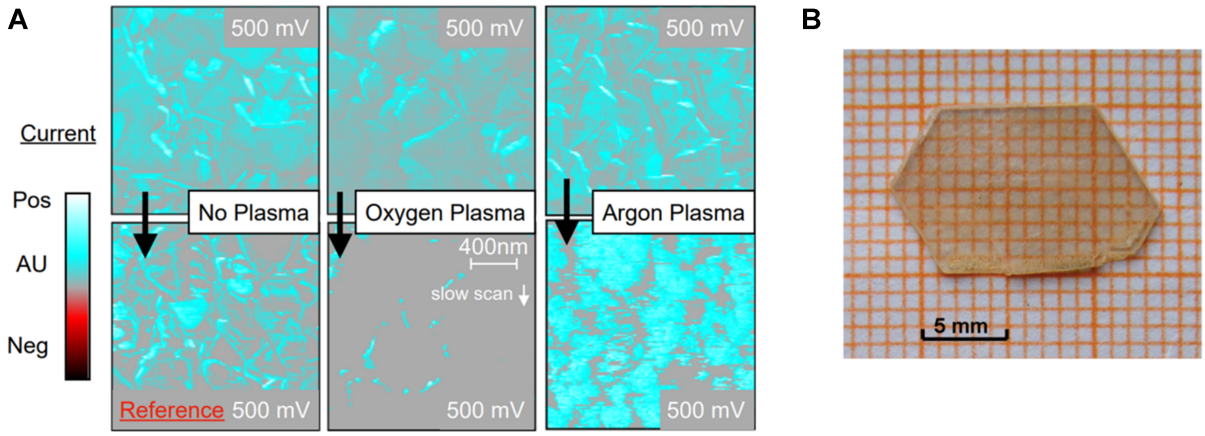

Figure 9. (A) Investigation of the influence of O on CuI thin films using current probe atomic force microscopy, comparing CuI film without plasma treatment, and the films treated with O or argon plasma[119]. Copyright 2023 John Wiley & Sons, Inc; (B) Photograph of a single crystal CuI (15 mm × 10 mm × 1 mm)[32]. Copyright 2010 American Chemical Society. CuI: Copper iodide.

INTERLAYER FOR OPTOELECTRONICS

CuI possesses favorable features for HTL or hole injection layer (HIL) due to its very fast carrier dynamics at high carrier densities. In 2022, Li *et al.* investigated the carrier dynamics of CuI, revealing that CuI exhibits picosecond fast absorption and a slow cool down rate of hot carriers under high carrier density [Figure 10]. The slow cool down is attributed to Auger heating and the hot phonon bottleneck effect. These properties make CuI suitable for application in HTL or HIL, as it combines high carrier concentration, fast recombination rates, a slow cool down rate of hot carriers, a large bandgap, and high transmittance[120].

Organic light-emitting diode

OLEDs have garnered interest due to their high-quality image display, thin thickness that allows for various screen forms, as well as their transparency and flexibility[121,122]. Achieving high efficiency and long lifetime in OLEDs requires an appropriate HTL or HIL[123]. CuI HIL is known to have the highest occupied molecular orbital (HOMO) and the lowest unoccupied molecular orbital (LUMO) energy levels of 5.2 and 2.1 eV, respectively [Figure 11A], and an absorption wavelength of 410 nm[124,125]. Lee *et al.* reported on a CuI-doped HIL, where a doping concentration of 20% resulted in the turn-on voltage shifting from 10 to 2.9 V. Additionally, OLED devices with a 20% CuI-doped HIL layer exhibited a maximum current efficiency (CE_{max}) of 69 cd·A^{-1} and an EQE of 17.5% at 0.14 mA·cm^{-2}. These results indicated that CuI doping enhances OLED performance by forming a charge transfer complex in the HIL[126].

Stakhira *et al.* investigated a CuI injection layer for OLEDs, comparing structures with and without a CuI HIL. The OLED with the CuI layer required a lower voltage for the same current density and efficiency. Specifically, the OLED with a CuI HIL needed only 6 V for 20 mA·cm^{-2}, while the OLED without a CuI HIL required 8.5 V. The CE_{max} of the OLED with a CuI HIL was enhanced by 34%, reaching 2.86 cd·A^{-1}. They confirmed that the CuI layer can effectively lower the potential barrier for hole injection[124]. Hotra *et al.* studied the effect of CuI HIL thickness on OLED properties, noting that the properties are significantly influenced by both HIL and electron injection layer (EIL) thickness. They tested various CuI thicknesses of 0, 5, 8, 12, 18, and 30 nm. X-ray diffraction (XRD) measurement indicated that the deposited CuI had an amorphous structure. They revealed that the CuI layer reduces carrier traps and enhances hole injection. The optimal CuI thickness was found to be 12 nm, achieving a luminance of 4,000 cd·m^{-2} at a current density of 200 mA·cm^{-2}, which is an improvement compared to an OLED without the CuI layer (3,000 cd·m^{-2}). Beyond 12 nm, luminance decreased due to increased series resistance and resulting Joule heating[127].

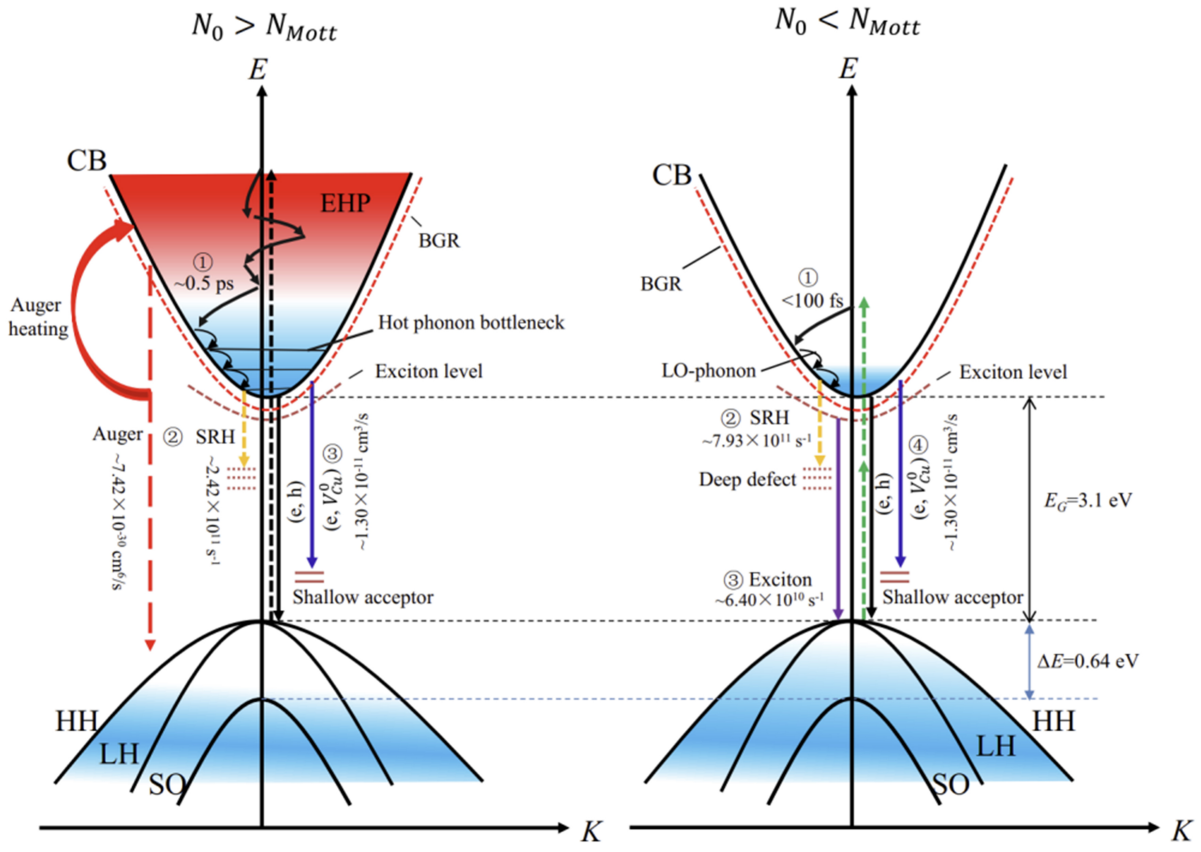

Figure 10. Schematic illustration of carrier dynamics in CuI under high and low carrier density conditions. Copyright 2022 Li *et al.*[120]. CuI: Copper iodide.

Choudhury *et al.* investigated nanocrystalline CuI HIL/HTL, which were made using a solution process dissolved in an ammonia-water solution, followed by low-temperature annealing at 110 °C. The annealed nanocrystalline CuI layer exhibited higher optical properties, better hole injection capability, and improved crystallinity compared to the CuI without annealing. A green OLED with the annealed nanocrystalline CuI showed a maximum EQE (EQE_{max}) of 17%, a maximum power efficiency (PE_{max}) of 64 lu·W^{-1}, and a CE_{max} of 62 cd·A^{-1}. These values are enhanced by 54%, 33%, and 15%, respectively, compared to a CuI layer without annealing. They also surpass the general HIL [poly(3,4-ethylenedioxythiophene) polystyrene sulfonate (PEDOT:PSS)] by 35%, 41%, and 38%, respectively [Figure 11B][128]. Table 4 indicates the summarized properties of CuI HIL OLEDs.

Solar cell

CuI-based HTLs have attracted attention due to their large bandgap, high conductivity, low cost, non-toxicity, solution processability, and high stability. Typically, PEDOT:PSS, poly[bis(4-phenyl)(2,4,6-trimethylphenyl)amine] (PTAA), 2,2',7,7'-Tetrakis(N,N-di-p-methoxyphenylamine)-9,9'-spirobifluorene (spiro-MeO-TAD), and poly(3-hexylthiophene-2,5-diyl) (P3HT) are used as HTLs for solar cells[131]. Here, we discuss various studies on CuI HTLs in organic solar cells, perovskite solar cells, and inverted perovskite solar cells, and compared their performance with typical HTLs.

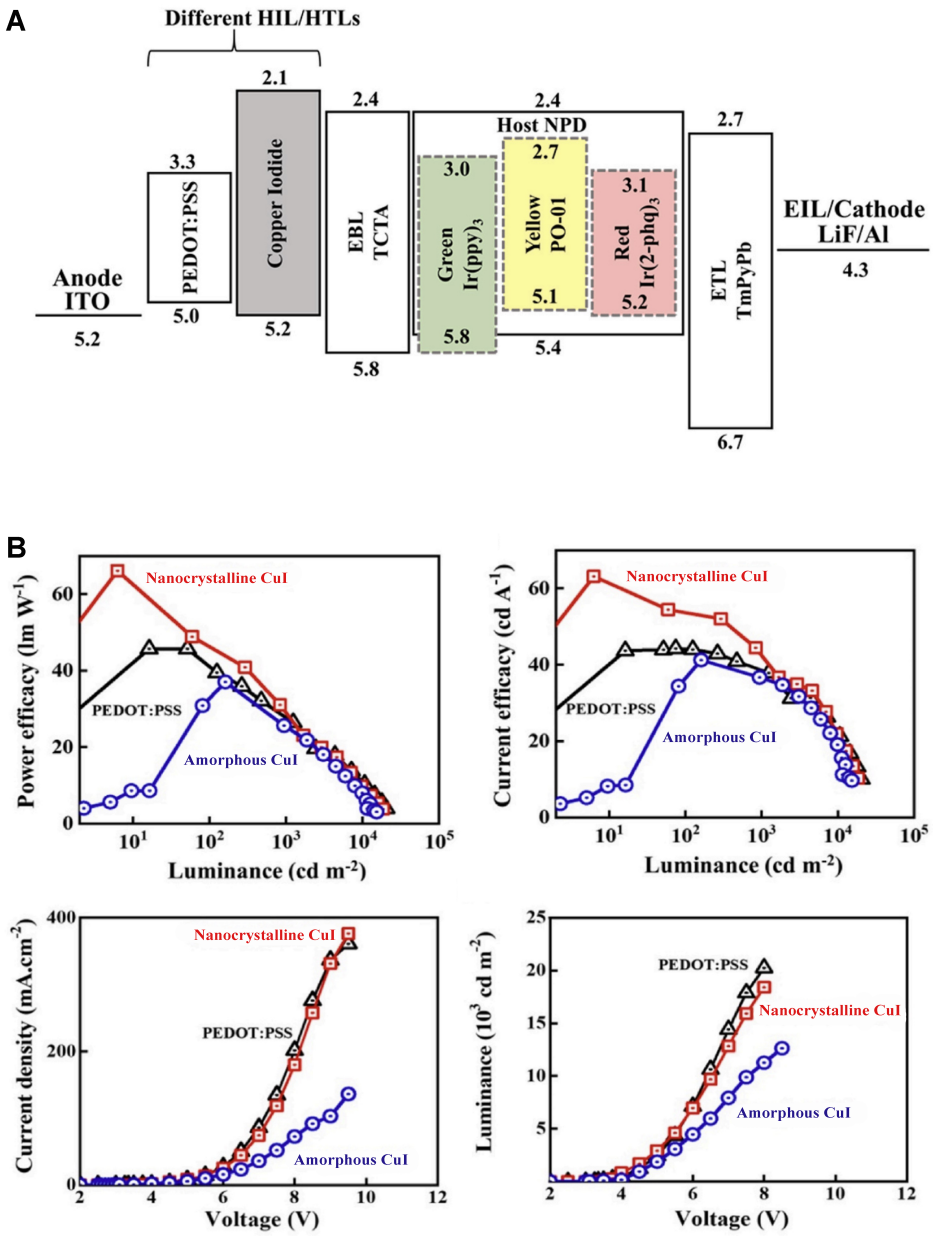

Figure 11. (A) Energy level diagram of the OLED with a CuI layer[128]. Copyright 2022 Elsevier B.V.; (B) OLED properties including power efficacy, current efficacy, current density, and luminance, comparing different types of HIL: nanocrystalline CuI, amorphous CuI, and PEDOT:PSS[128]. Copyright 2022 Elsevier B.V. OLED: Organic light emitting diode; CuI: copper iodide; HIL: hole injection layer; PEDOT:PSS: poly(3,4-ethylenedioxythiophene) polystyrene sulfonate.

Chen *et al.* reported the solution-processed, high-efficiency inverted planar heterojunction (PHJ) perovskite solar cells on flexible substrates with CuI-based HTLs. Although PEDOT:PSS is the most widely used HTL, its acidic and hygroscopic nature causes degradation and reduces the stability of the solar cells. In contrast, CuI offers low cost, solution processability, and hydrophobicity, which enhance both performance and stability. The power conversion efficiency (PCE) of devices with CuI HTLs was 13.58%, higher than that of solar cells with PEDOT:PSS (13.28%). Additionally, the stability of solar cells with CuI HTLs maintained 90% of their initial performance, while those with PEDOT:PSS maintained only 27%[35]. Sun *et al.* also reported on PHJ perovskite solar cells with CuI HTLs, comparing them to those with PEDOT:PSS HTLs.

Table 4. Summary of the characteristics of published data on OLEDs with CuI-based HIL

HIL materials	CE_{max} (cd·A^{-1})	EQE (%)	Year[ref.]
20% CuI-doped NPB	69	17.5	2008[126]
CuI	2.68	-	2010[124]
12 nm CuI	2[a]		2012[127]
10% CuI-doped *m*-MTDATA	10.4	-	2017[125]
25 wt.% CuI-doped CuSCN	16.8	-	2018[129]
CuI:CuPC	70	18.5	2020[130]
110 °C annealed nanocrystalline CuI	62	17	2022[128]

[a]4,000 cd·m^{-2} at 200 mA·cm^{-2}. OLEDs: CuI: Copper iodide; HIL: hole injection layer; EQE: external quantum efficiency; NPB: 1,4-bis[*N*-(1-naphthyl)-*N*′-phenylamino]-4,4′-diamine; *m*-MTDATA: 4,4′,4′′-tris(N-3-methylphenyl-N-phenyl-amino)triphenylamine; CuSCN: copper thiocyanate; CuPC: copper (II) phthalocyanine.

CuI was dissolved in ACN and spin-coated without post-annealing. In this study, the PCE of solar cells with CuI HTLs was 16.8%, while that of solar cells with PEDOT:PSS HTLs was 13.6%. These results suggest the potential of a CuI layer as a HTL for flexible solar cells due to its flexibility, low process temperature and acceptable electrical properties[132]. Hu *et al.* reported on perovskite solar cells with a CuI/PEDOT:PSS double layer for HTL. Their experiments indicated a higher PCE of 14.3% for the double layer, compared to 12.9% for the PEDOT:PSS single layer. The stability was also enhanced, with the initial performance maintaining around 88% after 720 h[133].

In 2018, Haider *et al.* conducted simulations on various HTL materials for perovskite solar cells. The results indicated that the PCE of devices with a CuI HTL could reach up to 21.32%. They compared PEDOT, PTAA, Spiro-MeOTAD, P3HT, and CuI. This paper compared the published experimental results; the PCEs of the devices with each HTL were similar, raging from 15% to 20% with Pb-based organic-inorganic hybrid perovskite photoactive layers. Although the PCE of solar cells with CuI (17.6%) was slightly lower than that with PTAA (20.2%), the cost of PTAA was more than 600 times higher than that of CuI. Moreover, the stability of CuI is also better than that of others. PEDOT:PSS, PTAA, and Spiro-MeOTAD are not stable with humidity, and P3HT is weak under heat[131]. In 2020, Haider *et al.* conducted simulations again on inverted perovskite solar cells with a CuI HTL, investigating the effects of hole carrier concentration, Hall mobility, and thickness. They optimized the carrier concentration to 1 × 10^{19} cm^{-3}, Hall mobility to 1 × 10^{-2} cm^2·V^{-1}·s^{-1}, defect density to 1 × 10^{14} cm^{-3}, and optical thickness to 100 nm. With these optimized conditions, the performance of the solar cell achieved a short-circuit current density (J_{SC}) of 20.08 mA·cm^{-2}, open circuit voltage (V_{OC}) of 1.17 V, fill factor (FF factor) of 89.45% and PCE of 21.32%. Regarding carrier concentration, the J_{SC} increased with carrier concentration and saturated at 1 × 10^{18} cm^{-3}. The carrier recombination rate and the energy band height also changed with carrier concentration. When the carrier concentration reached a sufficient level, the recombination rate no longer significantly affected performance, and the J_{SC} remained constant[134].

Khadka *et al.* reported on solar cells with an ammonia-aqueous solution-processed CuI HTL for a flexible substrate. They revealed that the morphology and crystallinity of the perovskite layer grown on the CuI layer were affected by the morphology of the CuI layer. They tested 0.025, 0.05, and 0.1 M CuI solutions, finding that the 0.05 M CuI solution produced the smoothest surface and best performance. The 0.025 M CuI solution resulted in a small grain size, while the 0.1 M CuI solution produced a rough surface. The PCE of the solar cell with an optimized CuI HTL reached 14.21%[135]. Mahdy *et al.* reported a CuI HTL fabricated using a solution iodination process with an iodine/ethanol solution for 1 h. They optimized the thickness of the CuI in an inverted planar perovskite solar cell, achieving a PCE of 0.76%. The relatively low

performance of the device might be attributed to the harsh annealing conditions (100 °C for 1 h), which induced many defects[136]. Aliyaselvam *et al.* reported a CuI HTL using a green solvent, monoethanolamide (MEA), applied for the first time as a CuI solvent. The optimized annealing temperature was 80 °C, resulting in high-density and uniform grains. Additionally, the crystallinity was higher than at other annealing temperatures, with an electrical conductivity of 28.38 $S \cdot cm^{-1}$. The performance of the solar cell with the CuI HTL showed a PCE of 21.37%, an FF of 82.77%, a J_{SC} of 22.74 $cmA \cdot cm^{-2}$, and V_{OC} of 1.14 V[137].

CuI HTLs are also used for organic solar cells, which are highly favorable in terms of flexibility, lightweight, environmental friendliness, and transparency. In 2015, Das *et al.* reported a CuI HTL in organic solar cells and compared various concentrations of CuI layers with PEDOT:PSS layers. The PCE was 2.33% for the PEDOT:PSS HTL, and with a 0.08 M CuI HTL, the PCE of the device was 2.25%[43]. Peng *et al.* conducted a similar experiment. They also compared the PCEs of solar cells with a CuI HTL and a PEDOT:PSS HTL. The CuI was dissolved in ACN, spin-coated, and annealed at 100 °C. The PCE with CuI was 5.54%, which was similar to the PCE with the PEDOT:PSS (5.50%)[138].

In 2021, Khatum *et al.* reported simulation results for a WS_2-based photovoltaic device. The PCE of the device without a CuI HTL was 22.09%, but with a CuI HTL, the PCE was enhanced to 29.87%. This improvement was attributed to the reduction of carrier recombination at the back surface with the CuI layer. They optimized the defect density between the absorption layer and HTL to 10^{11} cm^{-2}. Additionally, they asserted that increasing the doping density in the HTL could minimize carrier recombination[139]. The detailed solar cell properties according to the CuI HTL layer are summarized in Table 5.

THERMOELECTRIC DEVICES

Thermoelectric device

As a green energy source, CuI-based TEGs have garnered significant interest, particularly due to their transparent and flexible properties[141-143]. TEG is created using pairs of *p*-type and *n*-type semiconductors, and its performance is evaluated using the figure of merit (zT). The zT is calculated based on electrical conductivity, Seebeck coefficient, and thermal conductivity. These parameters are interrelated, making it challenging to control and enhance each value simultaneously. CuI has emerged as a promising *p*-type material for transparent and flexible TEGs due to its reasonable price and non-toxic nature compared to existing TEG materials. In this chapter, we will investigate strategies to enhance the thermoelectric properties of CuI.

Mulla *et al.* investigated the thermoelectric properties of CuI bulk pellets. The CuI powder was synthesized through a solution iodination process with iodine in ethanol, followed by different annealing conditions, ranging from no annealing to annealing temperatures between 373 and 573 K. They found that the electrical resistivity increased with higher annealing temperatures, and the Seebeck coefficient also rose from 431 to 1,490 $\mu V \cdot K^{-1}$[144]. Yang *et al.* produced CuI thin-film by sputtering with iodine vapor during deposition. They measured the electrical properties, Seebeck coefficient, thermal conductivity, and even transmittance and flexibility. The carrier concentration of CuI was controlled by varying the iodine pressure during deposition. Generally, thermoelectric properties are optimized when the trade-off is balanced; as the carrier concentration increases, electrical conductivity rises while the Seebeck coefficient decreases. The zT value was optimized to 0.21 at a carrier concentration of approximately 10^{20} cm^{-3}. As shown in Figure 12A, the thermal conductivity ranged from 0.5 to 0.56 $W \cdot m^{-1} \cdot K^{-1}$ with increasing carrier concentration. The relatively low thermal conductivity value of CuI was attributed to phonon scattering and the presence of heavy iodine atoms[27]. Coroa *et al.* fabricated 300 nm CuI thin films through iodination of thermally evaporated Cu thin films, achieving a zT of 0.29. The electrical conductivity was 110 $S \cdot cm^{-1}$ with a carrier concentration of 1.7 ×

Table 5. Summary of the characteristics of published data on solar cells with CuI-based HTL

Absorber materials	HTL	J_{SC} (mA·cm^{-2})	V_{OC} (V)	Fill factor (%)	PCE (%)	Year[Ref.]
BHJ of PBDTTPD and $PC_{61}BM$	Spin-coated CuI	14.0	0.81	50	5.54	2015[138]
CH_3NH_3I	Spin-coated CuI	21.06	1.04	62.0	13.58	2015[35]
P_3HT:$PC_{61}BN$	Spin-coated CuI	8.71	0.59	44	2.25	2015[43]
$CH_3NH_3PbI_3$	Solution-processed CuI	22.6	0.99	71.3	16.0	2016[132]
$CH_3NH_3PbI_3$	CuI[a]	25.47	0.99	84.53	21.32	2018[131]
$CH_3NH_3PbI_3$	CuI/PEDOT:PSS double layer	20.5	0.92	76	14.3	2018[133]
$CH_3NH_3PbI_3$	CuI[a]	20.08	1.17	89.45	21.06	2020[134]
$CH_3NH_3PbI_{3-x}Cl_x$	Auqueous solution-processed CuI	19.39	0.99	74	14.21	2020[135]
WS_2	CuI[a]	35.19	0.98	87.08	29.87	2021[139]
$CH_3NH_3PbI_3$	Spin-coated CuI	33	0.63	65	13.64	2023[140]
$CH_3NH_3PbI_3$	Spin-coated CuI with green solvent[b]	22.74	1.14	82.77	21.37	2023[137]
Complex perovskite	Iodinated CuI from sputtered Cu_3N	4.56	0.494	34	0.76	2023[136]

[a]Simulation results (not experimental). [b]Green solvent: monoethanolamine (MEA). CuI: Copper iodide; HTL: hole transport layer; PCE: power conversion efficiency; BHJ of PBDTTPD and $PC_{61}BM$: bulk-heterojunction (BHJ) blends of poly(di(2-ethylhexyloxy)benzo[1,2-b:4,5-b']dithiophene-co-octylthieno[3,4-c]porrole-4,6-dione) (PBDTTPD) and [6,6]-phenyl-C61-butyric acid methyl ester ($PC_{61}BM$); P_3HT:$PC_{61}BN$: poly(3-hexylthiophene):[6,6]-phenyl C61-butyric acid methyl ester.

10^{20} cm^{-3} and a Hall mobility of 4.1 cm^2·V^{-1}·s^{-1}. The Seebeck coefficient of CuI was 206 μV·K^{-1}, and the thermal conductivity was 0.48 W·m^{-1}·K^{-1}. They constructed a TEG using CuI and GZO as *p-n* modules on a Kapton substrate, confirming its flexibility and output power [Figure 12B]. In the compressive mode of the CuI films, the resistivity changed by less than 5%, while in tension mode, it changed by up to 9.1%. The maximum output power was 10.83 nW at a 20 °C temperature difference with 17 *p-n* modules[142]. Klochko *et al.* reported on CuI thin films produced by successive ionic layer absorption and reaction (SILAR). They confirmed that CuI thin films could be deposited using SILAR method on flexible PET substrates. By modifying the deposition conditions, they achieved a Seebeck coefficient ranging from 85 to 123 μV·K^{-1}. A single thermoleg exhibited an output power of 17.1 μW·m^{-2} at a 35 K temperature difference[145].

Murmu *et al.* suggested a method to enhance the Seebeck coefficient in CuI by annealing. They asserted that annealing creates Cu^0 defects in the CuI films, which act as potential barriers and energy filters. Additionally, annealing reduces carrier density. They achieved a high Seebeck coefficient of 789.6 μV·K^{-1}, but the electrical conductivity decreased to 11.8 S·cm^{-1}[146]. In another study, the same group further investigated the effect of annealing on CuI films to enhance the Seebeck coefficient. They reported a Seebeck coefficient of 561.8 μV·K^{-1}, which was higher compared to the non-annealed CuI (244.9 μV·K^{-1}). However, the electrical conductivity decreased from 22.9 to 14.0 S·cm^{-1} after annealing[146].

Murmu *et al.* also tried to enhance the thermoelectric properties through doping. They reported that sulfur ion implantation in CuI enhanced both electrical conductivity and the Seebeck coefficient. They increased the carrier concentration with sulfur doping from 2.4×10^{19} to 1.6×10^{20} cm^{-3}. They asserted that sulfur doping increased ionized impurities, which led to enhanced impurity scattering. This is significant as it helped overcome the trade-off relationship between electrical conductivity and the Seebeck coefficient. Electrical conductivity rose from 21.2 S·cm^{-1} before doping to 42.3 S·cm^{-1} after doping. The Seebeck coefficient increased from 255.5 to 498.6 μV·K^{-1} under optimized conditions[147]. Markwitz *et al.* fabricated $CuI_{(1-x)}Te_{(x)}$ thin films with various concentrations of Te. As the Te doping concentration increased, electrical conductivity decreased from 84 to 4 S·cm^{-1}, and the mobility of the films declined from 6.9 to 0.7 cm^2·V^{-1}·s^{-1}. However, the Seebeck coefficient increased from 232 to 293.4 μV·K^{-1}. They explained that Te doping resulted in smaller CuI grain sizes and induced GB scattering, which reduced carriers[47].

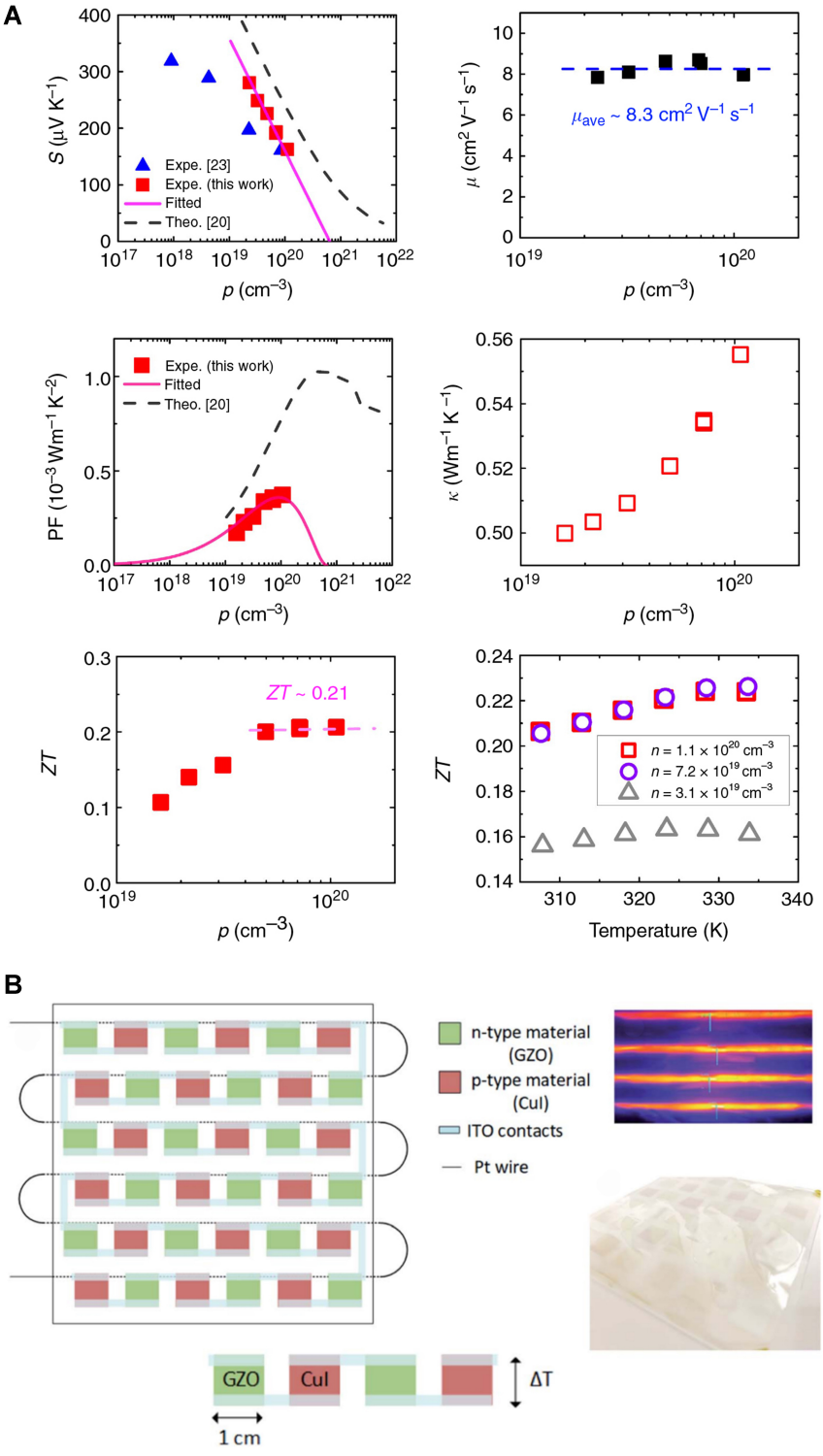

Figure 12. (A) Electrical and thermoelectrical properties of CuI thin film as a function of carrier concentration[27]. Copyright 2017 The Authors. Published by Springer Nature; (B) Schematic and photograph showcasing the transparency and flexibility of CuI and GZO-based TEG[142]. Copyright 2019 The Authors. Published by Royal Society of Chemistry. CuI: Copper iodide; GZO: Ga-Zn-O; TEG: thermoelectric generator.

Table 6. Summary of the characteristics of published data on CuI for TEGs

Materials	Electrical conductivity ($S \cdot cm^{-1}$)	Seebeck coefficient ($\mu V \cdot K^{-1}$)	Power factor ($\mu W \cdot m^{-1} \cdot K^{-2}$)	Thermal conductivity ($W \cdot m^{-1} \cdot K^{-1}$)	Measurement temperature (K)	zT	Year[Ref.]
I doped CuI	-	172	375	0.55	300	0.21	2017[27]
CuI (300 nm thick)	110	206	-	0.48	-	0.29	2019[142]
CuI with 0.05 M NaI precursor	-	115	66.1	-	RT	-	2019[145]
100 °C annealed CuI (Ar atmosphere)	11.8	789.	740.9	-	RT	-	2020[146]
Vacuum annealing	-	561.8	443.5	-	RT	-	2021[146]
S implanted CuI	25.9	498.6	642.9	-	RT	-	2022[147]
I doping CuI	5.43	308	-	-	RT	-	2022[150]
CuI	84.22	232.1	454	-	RT	-	2023[47]
Two-step annealed CuI	152	711	66	-	412	-	2023[56]
I doped CuI	207.6	180.1	673.3	0.66	RT	0.31	2023[148]

CuI: Copper iodide; TEGs: thermoelectric generators; RT: room temperature.

In 2023 and 2024, numerous researchers studied CuI thin films for TEG applications from various perspectives. Darnige *et al.* fabricated CuI thin films using a solid iodination method and annealed the films under specific conditions. They found that the optimal annealing conditions for stable electrical conductivity were 300 °C annealing in an Ar atmosphere flowed by 150 °C annealing in the air. This annealing process induced structural rearrangement, reducing Cu defects, and the air annealing introduced O doping, slightly increasing electrical conductivity. The electrical conductivity stabilized at 152 $S \cdot cm^{-1}$. The Seebeck coefficient was measured across different temperatures, ranging from 287 $\mu V \cdot K^{-1}$ at 44 °C to 711 $\mu V \cdot K^{-1}$ at 139 °C[56]. Bae *et al.* reported on iodine-doping CuI thin films and developed transparent and flexible thermoelectric devices. The CuI thin film was fabricated by spray coating with additional iodine in the precursor to achieve stoichiometric balance. They achieved an electrical conductivity of 207 $S \cdot cm^{-1}$ and a Seebeck coefficient of 180.1 $\mu V \cdot K^{-1}$. The optimized power factor was 673.3 $\mu W \cdot m^{-1} \cdot K^{-2}$, and the zT was 0.31[148]. Thimont *et al.* investigated CuI-based thermoelectric devices. The CuI film was made via an iodination process, and they optimized the module length and number through modeling based on experimental results of electrical conductivity and the Seebeck coefficient across various temperatures. The electrical conductivity and Seebeck coefficient ranged from around 35 to 55 $S \cdot cm^{-1}$ and 400 to 800 $\mu V \cdot K^{-1}$, respectively. The thermoelectric device modules were optimized with a length of 13 mm and three tracks. While increasing the length or number of tracks increased the V_{OC}, it also raised internal resistance[149]. Table 6 indicates the summarized properties of CuI TEGs.

CONCLUSION AND OUTLOOK

In this paper, we investigated recent progress of CuI for electronics, optoelectronics, and energy applications, as a transparent *p*-type semiconductor. While metal oxides have been commercialized as transparent semiconductors with excellent electrical and optical properties as *n*-type materials, there has been a lack of suitable *p*-type semiconductors for several decades. CuI exhibits high electrical performance, transmittance, and flexibility, and can be fabricated using various methods. In addition to its excellent optoelectronic performance, its abundance on earth, low cost, and non-toxicity make CuI promising for industrial implementation. We examined the underlying physics that gives CuI its excellent electrical

properties and explored its applicability in various applications such as channel layers for TFTs, transparent conductive electrodes, interlayers for optoelectronics, and thermoelectric power generation.

Despite these remarkable advantages, the electrical conductivity and robustness of CuI remain inconsistent. Unstable iodine vacancy generation and shallow acceptor energy levels from copper vacancies or *p*-type dopants contribute to the instability of electrical conductivity and limit carrier concentrations. Additionally, the tendency of CuI to grow polycrystalline structures could result in uncontrollable grain growth and rough surfaces, degrading hole mobility. Many researchers are addressing these issues through various strategies and fundamental studies. These challenges highlight the significant potential for further enhancing the electrical properties of CuI, which make CuI comparable to transparent *n*-type metal oxide semiconductors.

DECLARATIONS

Authors' contributions

Structuring and writing the manuscript: Kim GH, Lee J
Editing the manuscript: Ahn K
Structuring and editing the manuscript: Kim MG

Availability of data and materials

Not applicable.

Financial support and sponsorship

This work was supported by the National Research Foundation of Korea (NRF) funded by the Ministry of Education (NRF-2023R1A2C2005451) and the Technology Innovation Program (RS-2023-00256870 and No. 20012617) funded by the Ministry of Trade, Industry & Energy (MOTIE, Korea).

Conflicts of interest

Kim MG is the guest editor of the Special Issue, while the other authors have declared that they have no conflicts of interest.

Ethical approval and consent to participate

Not applicable.

Consent for publication

Not applicable.

REFERENCES

1. Forrest SR. The path to ubiquitous and low-cost organic electronic appliances on plastic. *Nature* 2004;428:911-8. DOI PubMed
2. Zhang D, Huang T, Duan L. Emerging self-emissive technologies for flexible displays. *Adv Mater* 2020;32:e1902391. DOI PubMed
3. Chang S, Cheng P, Li G, Yang Y. Transparent polymer photovoltaics for solar energy harvesting and beyond. *Joule* 2018;2:1039-54. DOI
4. Lee HE, Park JH, Kim TJ, et al. Novel electronics for flexible and neuromorphic computing. *Adv Funct Mater* 2018;28:1801690. DOI
5. Kim BH, Staller CM, Cho SH, et al. High mobility in nanocrystal-based transparent conducting oxide thin films. *ACS Nano* 2018;12:3200-8. DOI PubMed
6. van Hest MFAM, Dabney MS, Perkins JD, Ginley DS, Taylor MP. Titanium-doped indium oxide: a high-mobility transparent conductor. *Appl Phys Lett* 2005;87:032111. DOI

7. Shi J, Zhang J, Yang L, Qu M, Qi DC, Zhang KHL. Wide bandgap oxide semiconductors: from materials physics to optoelectronic devices. *Adv Mater* 2021;33:e2006230. DOI PubMed
8. Kawazoe H, Yanagi H, Ueda K, Hosono H. Transparent *p*-type conducting oxides: design and fabrication of *p*-*n* heterojunctions. *MRS Bull* 2000;25:28-36. DOI
9. Yanagi H, Kawazoe H, Kudo A, Yasukawa M, Hosono H. Chemical design and thin film preparation of *p*-type conductive transparent oxides. *J Electroceram* 2000;4:407-14. DOI
10. Kawazoe H, Yasukawa M, Hyodo H, Kurita M, Yanagi H, Hosono H. P-type electrical conduction in transparent thin films of $CuAlO_2$. *Nature* 1997;389:939-42. DOI
11. Wang Z, Nayak PK, Caraveo-Frescas JA, Alshareef HN. Recent developments in *p*-type oxide semiconductor materials and devices. *Adv Mater* 2016;28:3831-92. DOI PubMed
12. Liu A, Zhu H, Kim MG, Kim J, Noh YY. Engineering copper iodide (CuI) for multifunctional *p*-type transparent semiconductors and conductors. *Adv Sci* 2021;8:2100546. DOI PubMed PMC
13. Zhang Z, Guo Y, Robertson J. Electronic structure of amorphous copper iodide: a *p*-type transparent semiconductor. *Phys Rev Mater* 2020;4:054603. DOI
14. Willis J, Claes R, Zhou Q, et al. Limits to hole mobility and doping in copper iodide. *Chem Mater* 2023;35:8995-9006. DOI PubMed PMC
15. Grosskreutz JC. Mechanical properties of metal oxide films. *J Electrochem Soc* 1969;116:1232-7. DOI
16. Kim MG, Kanatzidis MG, Facchetti A, Marks TJ. Low-temperature fabrication of high-performance metal oxide thin-film electronics via combustion processing. *Nat Mater* 2011;10:382-8. DOI PubMed
17. Yu X, Zeng L, Zhou N, et al. Ultra-flexible, "invisible" thin-film transistors enabled by amorphous metal oxide/polymer channel layer blends. *Adv Mater* 2015;27:2390-9. DOI PubMed
18. Lee S, Kang D, Oh I. Multilayered graphene-carbon nanotube-iron oxide three-dimensional heterostructure for flexible electromagnetic interference shielding film. *Carbon* 2017;111:248-57. DOI
19. Yun J, Wang W, Bae TS, et al. Preparation of flexible organic solar cells with highly conductive and transparent metal-oxide multilayer electrodes based on silver oxide. *ACS Appl Mater Interfaces* 2013;5:9933-41. DOI PubMed
20. Le MN, Baeg K, Kim K, et al. Versatile solution-processed organic–inorganic hybrid superlattices for ultraflexible and transparent high-performance optoelectronic devices. *Adv Funct Mater* 2021;31:2103285. DOI
21. Vidor FF, Meyers T, Wirth GI, Hilleringmann U. ZnO nanoparticle thin-film transistors on flexible substrate using spray-coating technique. *Microelectron Eng* 2016;159:155-8. DOI
22. Xiao F, Li Y, Zan X, Liao K, Xu R, Duan H. Growth of metal–metal oxide nanostructures on freestanding graphene paper for flexible biosensors. *Adv Funct Mater* 2012;22:2487-94. DOI
23. Ou LX, Liu MY, Zhu LY, Zhang DW, Lu HL. Recent progress on flexible room-temperature gas sensors based on metal oxide semiconductor. *Nanomicro Lett* 2022;14:206. DOI PubMed PMC
24. Liu X, Miao J, Liao L, Hu W. High-mobility transparent amorphous metal oxide/nanostructure composite thin film transistors with enhanced-current paths for potential high-speed flexible electronics. *J Mater Chem C* 2014;2:1201-8. DOI
25. Jeong JW, Hwang HS, Choi D, Ma BC, Jung J, Chang M. Hybrid polymer/metal oxide thin films for high performance, flexible transistors. *Micromachines* 2020;11:264. DOI PubMed PMC
26. Kang H, Jung S, Jeong S, Kim G, Lee K. Polymer-metal hybrid transparent electrodes for flexible electronics. *Nat Commun* 2015;6:6503. DOI PubMed PMC
27. Yang C, Souchay D, Kneiß M, et al. Transparent flexible thermoelectric material based on non-toxic earth-abundant *p*-type copper iodide thin film. *Nat Commun* 2017;8:16076. DOI PubMed PMC
28. Ahn K, Kim GH, Kim S, et al. Highly conductive *p*-type transparent conducting electrode with sulfur-doped copper iodide. *Chem Mater* 2022;34:10517-27. DOI
29. Mishra D, Mokurala K, Kumar A, Seo SG, Jo HB, Jin SH. Light-mediated multi-level flexible copper iodide resistive random access memory for forming-free, ultra-low power data storage application. *Adv Funct Mater* 2023;33:2211022. DOI
30. GrauŽinytė M, Botti S, Marques MAL, Goedecker S, Flores-Livas JA. Computational acceleration of prospective dopant discovery in cuprous iodide. *Phys Chem Chem Phys* 2019;21:18839-49. DOI PubMed
31. Jung HS, Eun K, Kim YT, Lee EK, Choa S. Experimental and numerical investigation of flexibility of ITO electrode for application in flexible electronic devices. *Microsyst Technol* 2017;23:1961-70. DOI
32. Chen D, Wang Y, Lin Z, et al. Growth strategy and physical properties of the high mobility *p*-type CuI crystal. *Cryst Growth Des* 2010;10:2057-60. DOI
33. Sun W, Peng H, Li Y, et al. Solution-processed copper iodide as an inexpensive and effective anode buffer layer for polymer solar cells. *J Phys Chem C* 2014;118:16806-12. DOI
34. Son M, Kim GH, Song O, et al. Dopant control of solution-processed CuI:S for highly conductive *p*-type transparent electrode. *Adv Sci* 2024;11:e2308188. DOI PubMed PMC
35. Chen W, Deng L, Dai S, et al. Low-cost solution-processed copper iodide as an alternative to PEDOT:PSS hole transport layer for efficient and stable inverted planar heterojunction perovskite solar cells. *J Mater Chem A* 2015;3:19353-9. DOI
36. Kaushik DK, Selvaraj M, Ramu S, Subrahmanyam A. Thermal evaporated copper iodide (CuI) thin films: a note on the disorder evaluated through the temperature dependent electrical properties. *Sol Energy Mater Sol Cells* 2017;165:52-8. DOI

37. Storm P, Bar MS, Benndorf G, et al. High mobility, highly transparent, smooth, *p*-type CuI thin films grown by pulsed laser deposition. *APL Mater* 2020;8:091115. DOI
38. Yang C, Kneiβ M, Lorenz M, Grundmann M. Room-temperature synthesized copper iodide thin film as degenerate *p*-type transparent conductor with a boosted figure of merit. *Proc Natl Acad Sci U S A* 2016;113:12929-33. DOI PubMed PMC
39. Yamada N, Ino R, Ninomiya Y. Truly transparent *p*-type γ-CuI thin films with high hole mobility. *Chem Mater* 2016;28:4971-81. DOI
40. Lee HA, Yatsu K, Kim TI, Kwon HI, Park IJ. Synthesis of vacancy-controlled copper iodide semiconductor for high-performance *p*-type thin-film transistors. *ACS Appl Mater Interfaces* 2022;14:56416-26. DOI PubMed
41. Bädeker K. Über die elektrische Leitfähigkeit und die thermoelektrische Kraft einiger Schwermetallverbindungen. *Annalen der Physik* 1907;327:749-66. DOI
42. Liu A, Zhu H, Park WT, et al. Room-temperature solution-synthesized *p*-type copper(I) iodide semiconductors for transparent thin-film transistors and complementary electronics. *Adv Mater* 2018;30:e1802379. DOI PubMed
43. Das S, Choi J, Alford T. P3HT:PC61BM based solar cells employing solution processed copper iodide as the hole transport layer. *Sol Energy Mater Sol Cells* 2015;133:255-9. DOI
44. Choi CH, Gorecki JY, Fang Z, et al. Low-temperature, inkjet printed p-type copper(I) iodide thin film transistors. *J Mater Chem C* 2016;4:10309-14. DOI
45. Lee K, Gyu Oh J, Kim D, et al. Copper iodide and oxide semiconductor thin films patterned by spray-spin coating for fabricating complementary inverters: Improving stability with passivation layers. *Appl Surf Sci* 2023;608:155081. DOI
46. Mirza AS, Pols M, Soltanpoor W, Tao S, Brocks G, Morales-masis M. The role of sulfur in sulfur-doped copper(I) iodide *p*-type transparent conductors. *Matter* 2023;6:4306-20. DOI
47. Markwitz M, Murmu PP, Back SY, Mori T, Ruck BJ, Kennedy J. Effect of grain boundary scattering on carrier mobility and thermoelectric properties of tellurium incorporated copper iodide thin films. *Surf Interfaces* 2023;41:103190. DOI
48. Yu J, Han W, Suleiman AA, Han S, Miao N, Ling FC. Recent advances on pulsed laser deposition of large-scale thin films. *Small Methods* 2024;8:e2301282. DOI PubMed
49. Geng F, Wu YN, Splith D, et al. Amorphous transparent Cu(S,I) thin films with very high hole conductivity. *J Phys Chem Lett* 2023;14:6163-9. DOI PubMed
50. Keen DA, Hull S. The high-temperature structural behaviour of copper(I) iodide. *J Phys Condens Matter* 1995;7:5793-804. DOI
51. Kaindl G, Nowik I, Frank KH. High-pressure phases of CuI studied by ^{129}I-Mössbauer spectroscopy. *Hyperfine Interact* 1992;72:251-7. DOI
52. Yu H, Cai X, Yang Y, Wang Z, Wei S. Band gap anomaly in cuprous halides. *Comp Mater Sci* 2022;203:111157. DOI
53. Tanaka I, Kim D, Nakayama M, Nishimura H. Photoluminescence from heavy-hole and light-hole excitons split by thermal strain in CuI thin films. *J Lumin* 2000;87-9:257-9. DOI
54. Wang J, Li J, Li SS. Native *p*-type transparent conductive CuI via intrinsic defects. *J Appl Phys* 2011;110:054907. DOI
55. Jaschik S, Marques MRG, Seifert M, Rödl C, Botti S, Marques MAL. Stable ordered phases of cuprous iodide with complexes of copper vacancies. *Chem Mater* 2019;31:7877-82. DOI
56. Darnige P, Thimont Y, Presmanes L, Barnabé A. Insights into stability, transport, and thermoelectric properties of transparent p-type copper iodide thin films. *J Mater Chem C* 2023;11:630-44. DOI
57. Yamada N, Tanida Y, Murata H, Kondo T, Yoshida S. Wide-range-tunable *p*-type conductivity of transparent $CuI_{1-x}Br_x$ alloy. *Adv Funct Mater* 2020;30:2003096. DOI
58. Schein F, von Wenckstern H, Grundmann M. Transparent *p*-CuI/*n*-ZnO heterojunction diodes. *Appl Phys Lett* 2013;102:092109. DOI
59. Yang C, Kneiß M, Schein FL, Lorenz M, Grundmann M. Room-temperature domain-epitaxy of copper iodide thin films for transparent CuI/ZnO heterojunctions with high rectification ratios larger than 10^9. *Sci Rep* 2016;6:21937. DOI PubMed PMC
60. Zuo C, Cai S, Li Z, Fang X. A transparent, self-powered photodetector based on *p*-CuI/n-TiO_2 heterojunction film with high on-off ratio. *Nanotechnology* 2021;33:105202. DOI PubMed
61. Cha JH, Jung DY. Air-stable transparent silver iodide-copper iodide heterojunction diode. *ACS Appl Mater Interfaces* 2017;9:43807-13. DOI PubMed
62. Kim T, Son C, Lee J, et al. Interfacial ZnS passivation for improvement of transparent ZnO/CuI diode characteristics. *Appl Surf Sci* 2021;536:147645. DOI
63. Lee JH, Lee WJ, Kim TH, Lee T, Hong S, Kim KH. Transparent *p*-CuI/*n*-$BaSnO_{3-\delta}$ heterojunctions with a high rectification ratio. *J Phys Condens Matter* 2017;29:384004. DOI
64. Yamada N, Kondo Y, Ino R. Low-temperature fabrication and performance of polycrystalline CuI films as transparent *p*-type semiconductors. *Phys Status Solidi A* 2019;216:1700782. DOI
65. Lee JH, Lee BH, Kang J, et al. Characteristics and electronic band alignment of a transparent *p*-CuI/n-SiZnSnO heterojunction diode with a high rectification ratio. *Nanomaterials* 2021;11:1237. DOI PubMed PMC
66. Grundmann M, Schein F, Lorenz M, Böntgen T, Lenzner J, von Wenckstern H. Cuprous iodide - a *p*-type transparent semiconductor: history and novel applications. *Phys Status Solidi A* 2013;210:1671-703. DOI
67. Xiong C, Yao R. Low temperature preparation p-CuI/n-ZnO wide gap heterojunction diode. *Optik* 2015;126:1951-4. DOI
68. Ayhan ME, Shinde M, Todankar B, et al. Ultraviolet radiation-induced photovoltaic action in γ-CuI/β-Ga_2O_3 heterojunction. *Mater*

Lett 2020;262:127074. DOI
69. Weiß A, Goldmann J, Kettunen S, et al. Conversion of ALD CuO thin films into transparent conductive *p*-type CuI thin films. *Adv Mater Inter* 2023;10:2201860. DOI
70. Yang Z, Li M, Wang W, Gong J, Sun H, Sun H. Fabrication of transparent p-CuI/n-ZnO heterojunction with excellent ideality factor. *J Phys D Appl Phys* 2024;57:145301. DOI
71. Fortunato E, Martins R. Where science fiction meets reality? With oxide semiconductors! *Phys Status Solidi R* 2011;5:336-9. DOI
72. Fortunato E, Barros R, Barquinha P, et al. Transparent *p*-type SnOx thin film transistors produced by reactive rf magnetron sputtering followed by low temperature annealing. *Appl Phys Lett* 2010;97:052105. DOI
73. Ogo Y, Hiramatsu H, Nomura K, et al. *p*-channel thin-film transistor using *p*-type oxide semiconductor, SnO. *Appl Phys Lett* 2008;93:032113. DOI
74. Ogo Y, Hiramatsu H, Nomura K, et al. Tin monoxide as an *s*-orbital-based *p*-type oxide semiconductor: electronic structures and TFT application. *Phys Status Solidi* 2009;206:2187-91. DOI
75. Zhang KH, Xi K, Blamire MG, Egdell RG. P-type transparent conducting oxides. *J Phys Condens Matter* 2016;28:383002. DOI PubMed
76. Klauk H, Gundlach DJ, Nichols JA, Jackson TN. Pentacene organic thin-film transistors for circuit and display applications. *IEEE T Electron Dev* 1999;46:1258-63. DOI
77. Park JH, Kang CH, Kim YJ, Lee YS, Choi JS. Characteristics of pentacene-based thin-film transistors. *Mater Sci Eng C* 2004;24:27-9. DOI
78. Zhou L, Park S, Bai B, et al. Pentacene TFT driven AM OLED displays. *IEEE Electron Device Lett* 2005;26:640-2. DOI
79. Reig M, Puigdollers J, Velasco D. Molecular order of air-stable *p*-type organic thin-film transistors by tuning the extension of the π-conjugated core: the cases of indolo[3,2-b]carbazole and triindole semiconductors. *J Mater Chem C* 2015;3:506-13. DOI
80. Liu A, Zhu H, Park WT, et al. High-performance p-channel transistors with transparent Zn doped-CuI. *Nat Commun* 2020;11:4309. DOI PubMed PMC
81. Li S, Liebe B, Son C, et al. Inkjet-printed p-type $CuBr_xI_{1-x}$: wearable thin-film transistors. *Mater Adv* 2022;3:7538-45. DOI
82. Rajani K, Daniels S, Rahman M, Cowley A, Mcnally P. Deposition of earth-abundant p-type CuBr films with high hole conductivity and realization of p-CuBr/n-Si heterojunction solar cell. *Mater Lett* 2013;111:63-6. DOI
83. Wei W, Gao M, Wang Z, et al. High-performance p-channel CuIBr thin-film transistor synthesized from solution in the atmosphere. *Appl Phys Lett* 2023;122:193301. DOI
84. Wu H, Liang L, Wang X, et al. High-mobility flexible/transparent p-type copper iodide thin-film transistors and complementary inverters. *Appl Surf Sci* 2023;612:155795. DOI
85. Lee H, Kim TI, Kwon H, Park I. Effects of solution processable CuI thin films with Al_2O_3-based sandwiched architecture for high-performance p-type transistor applications. *J Mater Chem C* 2024;12:6457-68. DOI
86. Dai M, Xu W. Polarization mechanism and quasi-electric-double-layer modeling for indium-tin-oxide electric-double-layer thin-film-transistors. *Appl Phys Lett* 2012;100:113506. DOI
87. Cho J, Lee J, He Y, Kim B, Lodge T, Frisbie C. High-capacitance ion gel gate dielectrics with faster polarization response times for organic thin film transistors. *Adv Mater* 2008;20:686-90. DOI
88. Liang X, Luo Y, Pei Y, Wang M, Liu C. Multimode transistors and neural networks based on ion-dynamic capacitance. *Nat Electron* 2022;5:859-69. DOI
89. Annadi A, Zhang N, Lim DBK, Gong H. Hole transport modulations in low dimensional γ-CuI films: implication for high figure of merit and thin film transistors. *ACS Appl Electron Mater* 2019;1:1029-37. DOI
90. Liu A, Zhu H, Shim KI, et al. Key roles of trace oxygen treatment for high-performance Zn-doped CuI p-channel transistors. *Adv Elect Mater* 2021;7:2000933. DOI
91. Wang M, Li H, Xin Q, et al. Performance enhancement of solution-processed p-type CuI TFTs by self-assembled monolayer treatment. *Appl Surf Sci* 2023;638:158075. DOI
92. Huang Y, Tan J, Gao G, et al. Transparent p-type CuI film based self-powered ultraviolet photodetectors with ultrahigh speed, responsivity and detectivity. *J Mater Chem C* 2022;10:13040-6. DOI
93. Tsay CY, Chen YC, Tsai HM, Sittimart P, Yoshitake T. The role of Zn substitution in improving the electrical properties of CuI thin films and optoelectronic performance of CuI MSM photodetectors. *Materials* 2022;15:8145. DOI PubMed PMC
94. Yamada N, Kondo Y, Cao X, Nakano Y. Visible-blind wide-dynamic-range fast-response self-powered ultraviolet photodetector based on CuI/In-Ga-Zn-O heterojunction. *Appl Mater Today* 2019;15:153-62. DOI
95. Li S, Zhang Y, Yang W, Fang X. Solution-processed transparent Sn^{4+}-doped CuI hybrid photodetectors with enhanced performances. *Adv Mater Interfaces* 2019;6:1900669. DOI
96. Cao F, Jin L, Wu Y, Ji X. High-performance, self-powered UV photodetector based on Au nanoparticles decorated ZnO/CuI heterostructure. *J Alloys Compd* 2021;859:158383. DOI
97. Cao F, Liu Y, Liu M, et al. Wide bandgap semiconductors for ultraviolet photodetectors: approaches, applications, and prospects. *Research* 2024;7:0385. DOI PubMed PMC
98. Burm J, Litvin KI, Woodard DW, et al. High-frequency, high-efficiency MSM photodetectors. *IEEE J Quantum Electron* 1995;31:1504-9. DOI
99. Shyam A, Amal Kaitheri N, Raju R, Swaminathan R. Self-powered UV photodetectors based on heterojunctions composed of ZnO

nanorods coated with thin films of ZnS and CuI. *ACS Appl Nano Mater* 2023;6:8529-39. DOI

100. Madusanka H, Herath H, Fernando C. High photoresponse performance of self-powered n-Cu_2O/p-CuI heterojunction based UV-visible photodetector. *Sensor Actuat A Phys* 2019;296:61-9. DOI
101. Zhou Z, Zhao F, Wang C, et al. Self-powered p-CuI/n-GaN heterojunction UV photodetector based on thermal evaporated high quality CuI thin film. *Opt Express* 2022;30:29749-59. DOI
102. Mahyavanshi RD, Desai P, Ranade A, Tanemura M, Kalita G. Observing charge transfer interaction in CuI and MoS_2 heterojunction for photoresponsive device application. *ACS Appl Electron Mater* 2019;1:302-10. DOI
103. Zhang Y, Li S, Yang W, Joshi MK, Fang X. Millimeter-sized single-crystal $CsPbrB_3$/CuI heterojunction for high-performance self-powered photodetector. *J Phys Chem Lett* 2019;10:2400-7. DOI PubMed
104. Li Z, Zhang L, Wang J, et al. Hydrothermal growth and their optoelectronic device application of CuI nanostructure. *Mater Res Express* 2019;6:045048. DOI
105. Niu S, Zhao F, Hang Y, et al. Enhanced p-CuI/n-ZnO photodetector based on thermal evaporated CuI and pulsed laser deposited ZnO nanowires. *Opt Lett* 2020;45:559-62. DOI
106. Krishnaiah M, Kumar A, Mishra D, Kushwaha AK, Jin SH, Park JT. Solution-processed CuI films towards flexible visible-photodetectors: role of annealing temperature on Cu/I ratio and photodetective properties. *J Alloy Compd* 2021;887:161326. DOI
107. Krishnaiah M, Kumar A, Kushwaha AK, Song J, Jin SH. Thickness dependent photodetection properties of solution-processed CuI films: towards cost-effective flexible visible photodetectors. *Mater Lett* 2021;305:130815. DOI
108. Cao N, Zhang L, Li X, et al. Self-powered deep ultraviolet photodetector based on p-CuI/n-$ZnGa_2O_4$ heterojunction with high sensitivity and fast speed. *Opt Express* 2024;32:11573-82. DOI PubMed
109. Storm P, Bar MS, Selle S, von Wenckstern H, Grundmann M, Lorenz M. p-Type doping and alloying of CuI thin films with selenium. *Phys Status Solidi R* 2021;15:2100214. DOI
110. Matsuzaki K, Tsunoda N, Kumagai Y, et al. Hole-doping to a Cu(I)-based semiconductor with an isovalent cation: utilizing a complex defect as a shallow acceptor. *J Am Chem Soc* 2022;144:16572-8. DOI
111. Raj V, Lu T, Lockrey M, et al. Introduction of TiO_2 in CuI for its improved performance as a p-type transparent conductor. *ACS Appl Mater Interfaces* 2019;11:24254-63. DOI PubMed
112. Xue R, Gao G, Yang L, Xu L, Zhang Y, Zhu J. High-performance p-type transparent conducting CuI-Cu_2O thin films with enhanced hole mobility, surface, and stability. *J Mater Chem C* 2023;11:13681-90. DOI
113. Inagaki S, Nakamura M, Aizawa N, et al. Molecular beam epitaxy of high-quality CuI thin films on a low temperature grown buffer layer. *Appl Phys Lett* 2020;116:192105. DOI
114. Crovetto A, Hempel H, Rusu M, et al. Water adsorption enhances electrical conductivity in transparent p-type CuI. *ACS Appl Mater Interfaces* 2020;12:48741-7. DOI PubMed
115. Lv Y, Xu Z, Ye L, Zhang Z, Su G, Zhuang X. Large γ-CuI semiconductor single crystal growth by a temperature reduction method from an NH_4I aqueous solution. *CrystEngComm* 2015;17:862-7. DOI
116. Peng W, Li L, Yu S, Yang P, Xu K, Luo W. High-performance flexible transparent p-CuI film by optimized solid iodization. *Vacuum* 2021;183:109862. DOI
117. Lee HJ, Park M, Lee S, Kim B, Hong K. Solution-processed copper iodide film as a *p*-type electrical conductor and their applications. *ACS Appl Electron Mater* 2022;4:1232-7. DOI
118. Cota-leal M, Cabrera-german D, Sotelo-lerma M, Martínez-gil M, García-valenzuela J. Highly-transparent and conductive CuI films obtained by a redirected low-cost and electroless two-step route: chemical solution deposition of CuS_2 and subsequent iodination. *Mat Sci Semicon Proc* 2019;95:59-67. DOI
119. Stralka T, Bar M, Schöppach F, et al. Grain and grain boundary conduction channels in copper iodide thin films. *Phys Status Solidi A* 2023;220:2200883. DOI
120. Li ZH, He JX, Lv XH, et al. Optoelectronic properties and ultrafast carrier dynamics of copper iodide thin films. *Nat Commun* 2022;13:6346. DOI PubMed PMC
121. Zou S, Shen Y, Xie F, Chen J, Li Y, Tang J. Recent advances in organic light-emitting diodes: toward smart lighting and displays. *Mater Chem Front* 2020;4:788-820. DOI
122. Xu R, Li Y, Tang J. Recent advances in flexible organic light-emitting diodes. *J Mater Chem C* 2016;4:9116-42. DOI
123. Shahnawaz S, Sudheendran Swayamprabha S, Nagar MR, et al. Hole-transporting materials for organic light-emitting diodes: an overview. *J Mater Chem C* 2019;7:7144-58. DOI
124. Stakhira P, Cherpak V, Volynyuk D, et al. Characteristics of organic light emitting diodes with copper iodide as injection layer. *Thin Solid Films* 2010;518:7016-8. DOI
125. Shan M, Jiang H, Guan Y, et al. Enhanced hole injection in organic light-emitting diodes utilizing a copper iodide-doped hole injection layer. *RSC Adv* 2017;7:13584-9. DOI
126. Lee J, Leem D, Kim J. High performance top-emitting organic light-emitting diodes with copper iodide-doped hole injection layer. *Organic Electronics* 2008;9:805-8. DOI
127. Hotra Z, Stakhira P, Cherpak V, et al. Effect of thickness of CuI hole injection layer on properties of organic light emitting diodes. *Photonics Lett Pol* 2012;4:35-7. Available from: https://photonics.pl/PLP/index.php/letters/article/view/4-13. [Last accessed on 13 Sep 2024]
128. Choudhury A, Nagar MR, The L, et al. Nanocrystalline copper iodide enabling high-efficiency organic LEDs. *Org Electron* 2022;111:106668. DOI

129. Luo W, Zeng C, Du X, et al. Copper thiocyanate/copper iodide based hole transport composites with balanced properties for efficient polymer light-emitting diodes. *J Mater Chem C* 2018;6:4895-902. DOI
130. Mohan V, Gautam AK, Choudhary SD, et al. Enhanced performance organic light emitting diode with CuI:CuPC composite hole transport layer. *IEEE Trans Nanotechnol* 2020;19:699-703. DOI
131. Haider SZ, Anwar H, Wang M. A comprehensive device modelling of perovskite solar cell with inorganic copper iodide as hole transport material. *Semicond Sci Technol* 2018;33:035001. DOI
132. Sun W, Ye S, Rao H, et al. Room-temperature and solution-processed copper iodide as the hole transport layer for inverted planar perovskite solar cells. *Nanoscale* 2016;8:15954-60. DOI PubMed
133. Hu W, Dall'agnese C, Wang X, et al. Copper iodide-PEDOT:PSS double hole transport layers for improved efficiency and stability in perovskite solar cells. *J Photoch Photobio A* 2018;357:36-40. DOI
134. Haider SZ, Anwar H, Manzoor S, Ismail AG, Wang M. A theoretical study for high-performance inverted p-i-n architecture perovskite solar cells with cuprous iodide as hole transport material. *Curr Appl Phys* 2020;20:1080-9. DOI
135. Khadka DB, Shirai Y, Yanagida M, Miyano K. Ammoniated aqueous precursor ink processed copper iodide as hole transport layer for inverted planar perovskite solar cells. *Sol Energy Mat Sol Cells* 2020;210:110486. DOI
136. Mahdy B, Isomura M, Kaneko T. Fabrication of inverted planar perovskite solar cells using the iodine/ethanol solution method for copper iodide as a hole transport layer. *Jpn J Appl Phys* 2023;62:SK1016. DOI
137. Aliyaselvam OV, Arith F, Mustafa AN, Chelvanathan P, Azam MA, Amin N. Incorporation of green solvent for low thermal budget flower-like copper(I) iodide (γ-CuI) for high-efficiency solar cell. *J Mater Sci Mater Electron* 2023;34:10578. DOI
138. Peng Y, Yaacobi-gross N, Perumal AK, et al. Efficient organic solar cells using copper(I) iodide (CuI) hole transport layers. *Appl Phys Lett* 2015;106:243302. DOI
139. Khatun MM, Sunny A, Ahmed SRA. Numerical investigation on performance improvement of WS_2 thin-film solar cell with copper iodide as hole transport layer. *Sol Energy* 2021;224:956-65. DOI
140. Srivastava M, Alheity MA, Yahya MZA, Singh RC, Gültekin SS. Conduction mechanism and photo-electrochemical performance of copper iodide hole transport material-based perovskite solar cell. *J Electron Mater* 2023;52:4351-8. DOI
141. Wang Y, Yang L, Shi XL, et al. Flexible thermoelectric materials and generators: challenges and innovations. *Adv Mater* 2019;31:e1807916. DOI PubMed
142. Coroa J, Morais Faustino BM, Marques A, et al. Highly transparent copper iodide thin film thermoelectric generator on a flexible substrate. *RSC Adv* 2019;9:35384-91. DOI PubMed PMC
143. Feng R, Tang F, Zhang N, Wang X. Flexible, high-power density, wearable thermoelectric nanogenerator and self-powered temperature sensor. *ACS Appl Mater Interfaces* 2019;11:38616-24. DOI
144. Mulla R, Rabinal MK. Defect-controlled copper iodide: a promising and ecofriendly thermoelectric material. *Energy Technol* 2018;6:1178-85. DOI
145. Klochko N, Zhadan D, Klepikova K, et al. Semi-transparent copper iodide thin films on flexible substrates as p-type thermolegs for a wearable thermoelectric generator. *Thin Solid Films* 2019;683:34-41. DOI
146. Murmu PP, Karthik V, Liu Z, et al. Influence of carrier density and energy barrier scattering on a high seebeck coefficient and power factor in transparent thermoelectric copper iodide. *ACS Appl Energy Mater* 2020;3:10037-44. DOI
147. Murmu PP, Kennedy J, Liu Z, Mori T. The role of sulfur valency on thermoelectric properties of sulfur ion implanted copper iodide. *J Alloy Compd* 2022;921:166103. DOI
148. Bae EJ, Kim J, Han M, Kang YH. Precision doping of iodine for highly conductive copper(I) iodide suitable for the spray-printable thermoelectric power generators. *ACS Mater Lett* 2023;5:2009-18. DOI
149. Thimont Y, Darnige P, Barnabé A. Development, experimental and simulated performance of copper iodide (γ-CuI) uni-track thin film thermoelectric modules. *Appl Surf Sci* 2024;649:159071. DOI
150. Vora-ud A, Chaarmart K, Kasemsin W, Boonkirdram S, Seetawan T. Transparent thermoelectric properties of copper iodide thin films. *Physica B* 2022;625:413527. DOI